POLITECNICO DI TORINO
Repository ISTITUZIONALE

Microstructural anisotropy and near-isotropic tribological behavior of electron beam powder bed fusion Ti–6Al–2Sn–4Zr–2Mo alloy

Original
Microstructural anisotropy and near-isotropic tribological behavior of electron beam powder bed fusion Ti–6Al–2Sn–4Zr–2Mo alloy / Davoodi, F., Taghian, M., Moazzen, P., Galati, M., Mohammadi, M., Saboori, A.. - In: PROGRESS IN ADDITIVE MANUFACTURING. - ISSN 2363-9512. - (2026). [10.1007/s40964-026-01717-5]

Availability:
This version is available at: 11583/3012827 since: 2026-07-08T10:55:58Z

Publisher:
Springer Nature

Published
DOI:10.1007/s40964-026-01717-5

Terms of use:

This article is made available under terms and conditions as specified in the corresponding bibliographic description in the repository

Publisher copyright

(Article begins on next page)

13 November 2026

Progress in Additive Manufacturing
https://doi.org/10.1007/s40964-026-01717-5

RESEARCH

Microstructural anisotropy and near-isotropic tribological behavior of electron beam powder bed fusion Ti–6Al–2Sn–4Zr–2Mo alloy

Farideh Davoodi[1] · Mohammad Taghian[2,3] · Parisa Moazzen[4] · Manuela Galati[2,3] · Mohsen Mohammadi[4] · Abdollah Saboori[2,3]

Received: 8 February 2026 / Accepted: 22 April 2026
© The Author(s) 2026

Abstract
Ti–6Al–2Sn–4Zr–2Mo (Ti6242) is a near-α titanium alloy developed for high-temperature applications, yet its tribological behavior in additively manufactured conditions remains insufficiently understood. This study aimed to investigate the influence of build orientation on the microstructure and tribological performance of Ti6242 components produced via electron beam powder bed fusion (EB-PBF) across temperatures from room temperature to 450 °C. The outcomes revealed that a higher fraction of equiaxed grains was observed in the horizontally oriented samples compared to the vertically oriented ones, reflecting the influence of build orientation on the microstructural anisotropy. Abrasive wear emerged as the predominant mechanism in EB-PBF-Ti6242 and Al_2O_3 ball interactions under all tested conditions. The tribological behavior at 450 °C exhibited characteristics comparable to those at room temperature, with a friction coefficient of approximately 0.5 and a wear volume about 10% lower than that measured at room temperature, may be attributed to the formation of a TiO_2 tribolayer. Although the horizontal sample possessed smaller porosities and slightly higher hardness than the vertical one, no significant wear anisotropy was observed under a 5 N load, due to the combined effects of microstructure, surface topography and local stress response. The similarity in tribological performance of Ti6242 alloy at different temperatures, regardless of build direction, underscores its uniform wear resistance across a wide range of operating conditions.

Keywords Additive manufacturing · Ti6242 alloy · Electron beam powder bed fusion · Wear anisotropy · Build direction

1 Introduction

Ti–6Al–2Sn–4Zr–2Mo (Ti6242) is a near-α titanium alloy known for its superior high-temperature performance compared to the widely used Ti6Al4V alloy [1, 2]. In this alloy, aluminium serves as an active α-stabilizing element, and Sn typically complements aluminium in enhancing solution strengthening. Mo is recognized as a primary β-stabilizing element, effectively lowering the β-transus temperature (T_β), and Zr is considered an α stabilizer due to its ability to

✉ Abdollah Saboori
Abdollah.saboori@polito.it

Farideh Davoodi
farideh.davoodi@poliba.it

Mohammad Taghian
mohammad.taghian@polito.it

Parisa Moazzen
parisa.moazzen@unb.ca

Manuela Galati
manuela.Galati@polito.it

Mohsen Mohammadi
Mohsen.Mohammadi@unb.ca

[1] Institute for Advanced Manufacturing (KSF), Furtwangen University, Tuttlingen, Germany

[2] Department of Management and Production Engineering, Polytechnic University of Turin, Turin, Italy

[3] Integrated Additive Manufacturing Center (IAM@PoliTo), Polytechnic University of Turin, Turin, Italy

[4] Marine Additive Manufacturing Centre of Excellence (MAMCE), University of New Brunswick, Fredericton, Canada

Published online: 13 May 2026

slow the transformation rate from α to β [3]. Ti6242 exhibits impressive tensile strength, toughness, and outstanding resistance to creep, fatigue, and corrosion. This alloy was found to be primarily used in power generation and aero-engine gas turbines, where tribological resistance is one of the most essential needs [4, 5].

The tribological behaviour of titanium alloys is governed by a combination of wear mechanisms that vary with temperature and microstructural state. At room temperature, titanium alloys typically exhibit the wear dominated by abrasion and delamination processes, while at high temperatures they are often associated with the formation of tribo-oxide or mechanically mixed layers on the contact surface. These surface layers, formed through the interaction of debris, oxygen and counterface material during sliding, can protect the substrate and maintain relatively low wear rates [6]. However, when the integrity of this layer is compromised—through cracking, spallation, or increased contact stress—the wear regime may transition to severe wear characterized [7]. At elevated temperatures, the dominant wear mechanisms evolve due to frictional heating, microstructural softening and enhanced oxidation kinetics. Increasing temperature promotes the formation of thicker oxide layers and intensifies thermally activated processes such as shear deformation and dynamic recrystallization [8]. Microstructure plays a key role in controlling these processes. For example, refined structures of Ti alloys typically characterized by fine α/β lamellae, or reduced grain size can increase hardness and improve deformation resistance, thereby enhancing wear performance compared with conventional microstructures [9]. In addition, the crystallographic orientation and grain morphology can significantly influence the dominant wear mechanisms [10].

Conventional manufacturing methods for Ti6242 face challenges such as internal defects from casting, oxygen pick-up, and machining difficulties due to its high-temperature strength [5]. Consequently, various strategies have been pursued to overcome these obstacles and enhance the application of the Ti6242 alloy in multiple industries [11].

To address these challenges, additive manufacturing (AM) has emerged as a promising alternative, offering several advantages over traditional methods. AM, particularly the electron beam powder bed fusion (EB-PBF) method, provides solutions for many conventional manufacturing challenges [12]. EB-PBF operates within a vacuum environment and leverages the high energy of an electron beam to preheat and melt the powder, enabling operation at high temperatures ranging from 50 to 70% of the material's melting point [13].

Despite all the advantages of the EB-PBF process, the inherent directional solidification in this process introduces anisotropy in the microstructure, as well as the mechanical and tribological properties of the as-built components [14]. It is well documented that this anisotropy can lead to significant performance issues, particularly in applications dealing with high stresses [15, 16]. It is also reported that the resulting anisotropic surface quality substantially impacts the tribological behaviour of the as-built components [17, 18]. As a matter of fact, when the wear rate of different surfaces of a part varies significantly due to anisotropy, it can negatively affect the dimension accuracy, shape, overall wear resistance, and finally, the lifetime of the part.

In addition, non-uniform wear can create stress concentrations within the part, and this imbalance in stress concentration distribution leads to structural weaknesses, crack formation, or complete early failure of the product [19, 20]. Therefore, if the wear and friction characteristics of distinct sections within an AM part, which can be characterized by different grain morphologies, exhibit similarity, this alignment can contribute to an extension in the lifetime of the component. Tool wear management is imperative for ensuring the production of high-quality machined components, enhancing production efficiency, and reducing costs. Consequently, it is crucial to gain a comprehensive understanding of how the anisotropic characteristics of AM components affect their machinability, which differs from that of conventionally produced ones [21, 22].

Some investigations have been undertaken regarding the anisotropic mechanical and tribological characteristics of AM outputs. For example, Walker et al. [23] examined the fatigue characteristics of laser powder bed fusion (L-PBF) produced Ti6Al4V and observed that vertically constructed samples exhibited greater average fatigue lifecycles compared to horizontally constructed ones. Conversely, in most of the past research on AM components, it has been observed that horizontal planes exhibit better mechanical properties than vertical ones. This advantage could be attributed to the equiaxed nature of grains in horizontally built samples, in contrast to the columnar grains manufactured vertically [24]. For instance, Lizuul et al. [21] observed a gradual decrease of up to 40% when transitioning from machining horizontally fabricated specimens to vertically manufactured ones during the tool lifespan of Ti6Al4V parts produced using L-PBF. Podgornik et al. [22] investigated the influence of the build direction (BD) on the anti-wear characteristics of maraging steel fabricated through L-PBF. Their results showed that the optimal synergy between abrasive and adhesive wear occurs in the horizontal direction with in-plane sliding, whereas sliding across the layers proves to be the most detrimental. Inclined printing at an angle of 45°, by contrast, circumvented anisotropy and delivered a favourable balance of high strength and toughness. More recently, Liu et al. [15] showed that the wear resistance and tribocorrosion

Table 1 Chemical composition of the starting Ti6242 powder

Chemical composition (wt%)	Al	Zr	Sn	Mo	Si	O	Ti
EDS analysis	5.93	3.96	2.20	2.11	0.14	–	Bal.
ICP-Inert gas fusion	6.08	3.29	1.80	1.58	0.05	0.14	Bal.

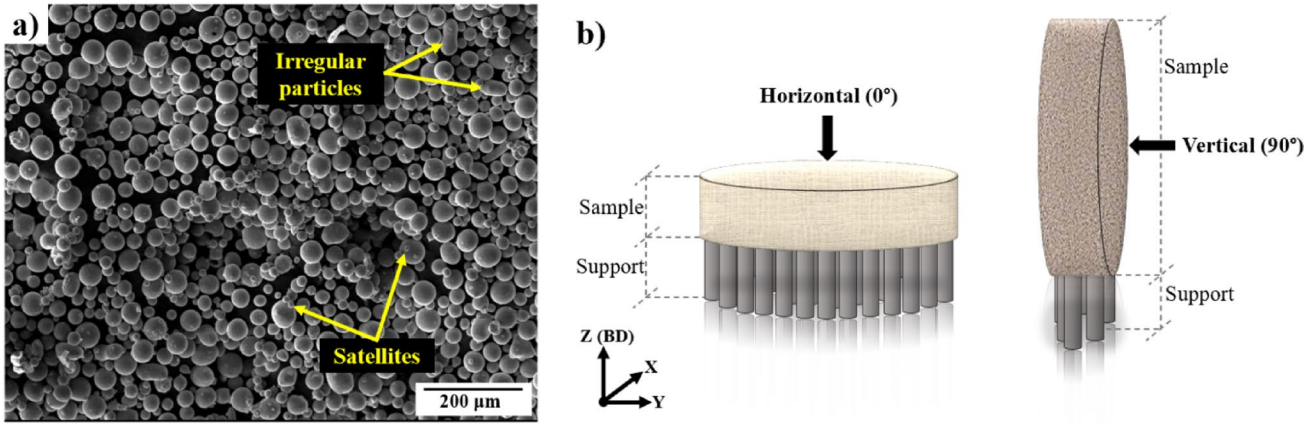


Fig. 1 **a** SEM image showcasing the initial Ti6242 powder morphology, **b** A schematic of the Ti6242 specimens fabricated using different build directions

performance of L-PBF-Ti6Al4V present superior results in the horizontal plane compared to the vertical plane.

Despite the growing use of additive manufacturing for high-performance titanium alloys, limited attention has been paid to the processability of Ti–6Al–2Sn–4Zr–2Mo (Ti6242) via the EB-PBF process and the actual fabrication of fully functional components from this alloy. Moreover, the influence of microstructural anisotropy on the wear and mechanical behavior of EB-PBF–processed Ti6242 remains largely unexplored, underscoring a significant gap in the current literature. Considering that Ti6242 is a preferred material for gas turbine compressor components, such as blades, discs, and impellers, operating at elevated temperatures around 450 °C [1], understanding its tribological behavior under such service conditions is of great importance. Therefore, this study aims to bridge this knowledge gap by systematically evaluating the tribological performance of EB-PBF-Ti6242 over a temperature range from room temperature to 450 °C, with particular emphasis on how build direction and resulting anisotropy govern its wear behavior.

2 Materials and methods

2.1 Sample production

Gas-atomized spherical Ti6242 alloy powders supplied by TLS Technik GmbH & Co was used as the starting material in this work. The morphology and chemical properties of the feedstock material were examined using a PhenomX secondary electron microscopy (SEM) with an energy-dispersive X-ray spectroscopy (EDS) analysis detector. Further verification was performed by inductively coupled plasma (ICP) analysis using Avio 500 ICP-OES by PerkinElmer and inert gas fusion using an ONH836 analyzer from LECO Europe BV, as detailed in Table 1. Based on the information presented in Table 1, the starting powder had a low oxygen concentration. The powder particle size range of the Ti6242 powder was between 45 and 106 µm, with a median diameter of approximately 75 ± 10 µm. Figure 1a displays the SEM micrograph of the initial powder, mainly consisting of spherical particles, although irregular particles and satellite coverage are also observed, which are the typical defects reported in the gas-atomized powders [25, 26]. It is well documented that the presence of these kinds of defects can deteriorate the flowability of the powder and, consequently, the quality of the as-built samples. Hence, more oversized outlet windows were utilized during machine setup to minimize these detrimental effects.

To analyze the wear resistance of the Ti6242 alloy, disk-shaped samples with 30 mm diameter and 5 mm thickness were designed following the ASTM G99 standards. In order to avoid direct contact between the as-built samples and the stainless steel start plate, the samples were printed 10 mm above the plate, and the relevant gap was filled using the support structure made of Ti6240 alloy. As illustrated in Fig. 1b, the various classes of the as-built specimens are denoted by horizontally oriented (0°) and vertically (90°) ones.

The Ti6242 samples were produced using an Arcam A2X EBM machine (software version 5.2.52). This process

involved standard settings like a 60 kV accelerating voltage and 50 µm layer thickness. The process began with preheating a stainless-steel start plate to 700 °C via electron beam scanning. Then, the powder was spread evenly on this preheated plate. Before starting the selective melting of the powder, each powder layer was preheated to sinter the powder and facilitate the conduction in the powder bed. This preheating and melting sequence was repeated in each layer until the sample production was completed. The focus and line offsets used in this work were 10 mA and 0.2 mm, respectively. The reference current and beam speed were set to 6 mA and 1060 mm/s, respectively. The entire EB-PBF process was conducted under strict temperature control, maintaining the temperature of the powder bed at a minimum of 580 °C. After the fabrication, any remaining un-melted powder was removed using an Arcam Powder recovery system (APRS). A schematic diagram of the EB-PBF process is illustrated in Fig. 2.

2.2 Material characterization

To mitigate the impact of surface roughness, all the as-built Ti6242 specimens were ground with abrasive SiC papers from #180 to #1200 and then washed with ethanol and distilled water. An X-ray diffractometer (XRD) of the ASENWARE (AW-XDM300 model) was utilized to analyze the phase composition and lattice parameters of the as-built specimens. The XRD analysis was performed with the X-rays generated with a Cu target at 40 kV, 30 mA, step time = 1 s, and step size = 0.05°.

To analyze the microstructure of the samples along the build direction using the optical microscope (OM, Nikon EPISHOT 300, Nikon, Tokyo, Japan), their surfaces were ground using abrasive papers ranging from grit size #180–#2400, followed by final polishing down to 1 micron using diamond paste. Afterwards, all the as-polished specimens underwent ultrasonic cleaning in ethanol and distilled water. In order to reveal the details of the microstructure, all the samples were chemically etched via immersion in Kroll's etching solution (6 Vol% HNO_3 and 3 vol% HF in water) for 10 s. To obtain a more detailed understanding of the crystallographic orientation, the microstructure of the samples were polished for 6 h using a vibratory polisher with an oxide polishing suspension (OPS) diluted in water. Comprehensive microstructural examination was conducted with a dual-beam FEI SCIOS 2 NICol field emission dual beam scanning electron microscope (SEM) equipped with a Symmetry® S3 EBSD detector (CMOS sensor) and operated via AZtecHKL software for EBSD acquisition. The collected data were subsequently processed and analyzed using OIM Analysis™ software.

To assess the density of the as-built Ti6242 samples, X-ray computer tomography (CT) measurements were carried out using a GE Phoenix v|tome|x S240 system. This high-resolution imaging tool, equipped with a 180 kV/20 W high-power nanofocus X-ray tube, enabled a superior resolution of 2500 × 3000 pixels at a pixel size of 100 µm. The average surface roughness of the samples (*Ra*) in different states was obtained utilizing an RTP-80 profilometer with a TL90 drive unit. The roughness values are an average based on five measurements.

Vickers microhardness assessments were performed to analyze the microhardness of the specimens using a Qness Q10 microhardness testing machine, applying a 5 N load for

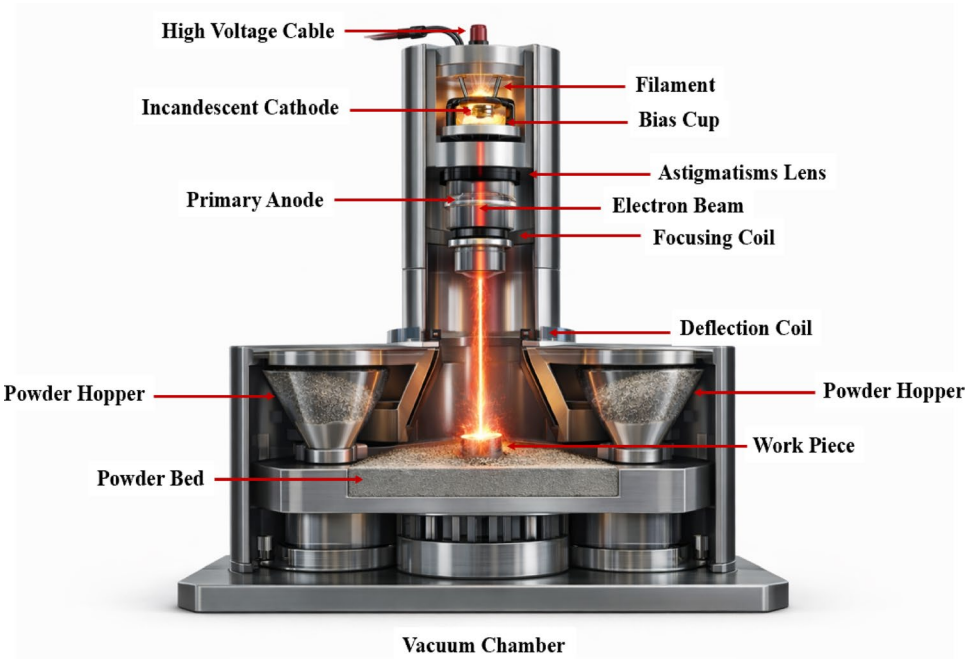


Fig. 2 Schematic diagram of the EB-PBF process

15 s. Each recorded hardness value represents the average of five measurements.

Comprehensive analysis of mechanical properties, including nano hardness and elastic modulus, was performed using a Nano-indenter (NHT2, CSM Instruments) equipped with a Berkovich-type diamond indenter. The indentation process was performed using a maximum load of 10 mN. To minimize experimental errors, each experiment was repeated at least five times at various locations, and the final result was derived from the average of five measurements.

Dry sliding wear tests were carried out using a ball-on-disk apparatus (CSM high-temperature wear tester) at three different temperatures: 25 °C, 250 °C, and 450 °C. The 25 °C is a baseline reference for evaluating the material's performance at room temperature. The 250 °C represents a moderate temperature commonly encountered in engineering applications, allowing for analysis of the changes in the alloy's mechanical and tribological behaviours before reaching high operational temperatures. Finally, the 450 °C reflects conditions typical in gas turbine compressor components, making it essential to understand the alloy's performance in real-world applications. In all experiments, the sliding speed of the disk was consistently maintained at 0.1 m/s, and a load of 5 N was applied for a total sliding duration of 30 min. The test configuration involved Ti6242 discs sliding against a 10 mm diameter alumina ball with a hardness of approximately 1500 HV. Each test was replicated three times to ensure reproducibility. Finally, the surfaces of the tested samples at various temperatures were examined using Zeiss EVO50 SEM-EDS. A schematic representation of the ball-on-disc setup used for the wear tests is presented in Fig. 3.

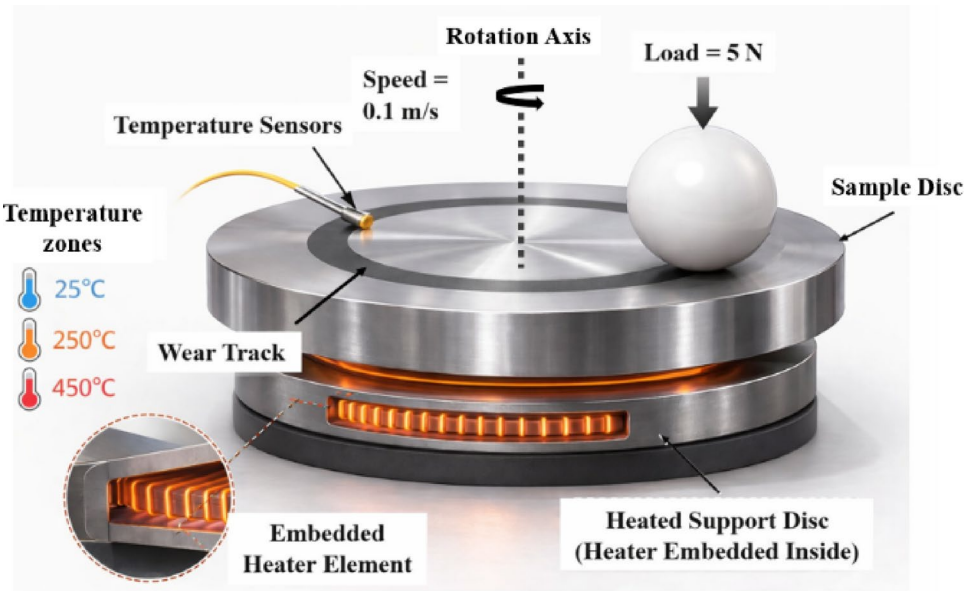


Fig. 3 Schematic diagram of the high-temperature ball-on-disc tribometer

3 Results and discussion

3.1 Porosity evaluation

Figure 4 reveals the porosity analysis of the Ti6242 specimen conducted using the XCT method. A colour-coded representation was employed to show the diameter of the porosities. The pores exhibit a concentration lower than 0.05%, underscoring the successful fabrication of Ti6242 alloy with a negligible defect content. The dimensions of porosities in the vertically built specimens surpass those in the horizontal ones. The green-teal voids, with a diameter of 500 ± 15 µm, are distinctly marked by yellow arrows in the XCT image. Conversely, the voids in the horizontally oriented specimens were less than 200 ± 15 µm. However, the porosity levels in horizontally oriented samples of elongated constructs exceed those in their vertically built counterparts. This variation in porosity can be attributed to the disparate thermal histories between vertically and horizontally constructed components [27, 28]. Although the link between build orientation, thermal history, and porosity is notably relevant, further research is required to fully understand how these factors interact with other process parameters. The pores act as stress concentration points within the EB-PBF parts, making it easier for cracks to initiate from these areas and propagate into the surrounding healthy regions, resulting in an early failure [29].

Following previous research findings [30, 31], the presence of larger pores raises more significant concerns than the scattered distribution of smaller pores. Larger pores may arise from inadequacies in the powder's layering process or incomplete melting during the manufacturing process. For example, according to the research conducted by Luo et al. [32] on PBF-Ti alloys, intermediate-sized pores, ranging

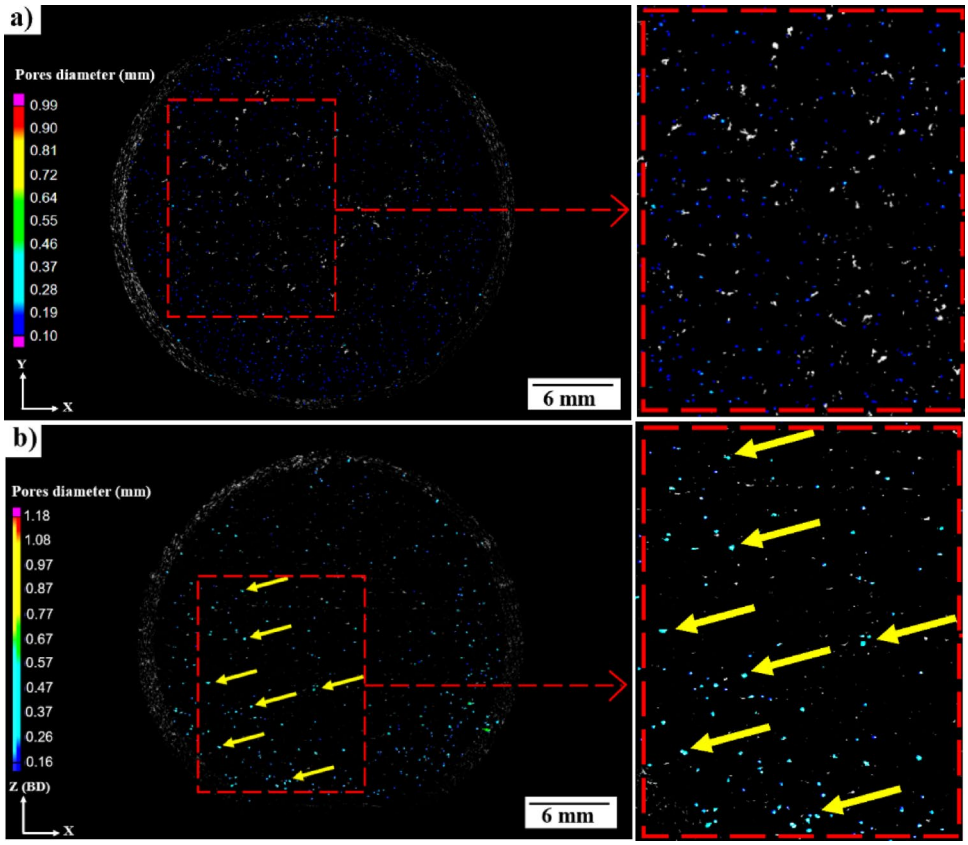


Fig. 4 Porosity distribution in **a** horizontally and **b** vertically oriented Ti6242 samples obtained via XCT method

from 50 to 200 µm in diameter, may slightly decrease the elongation and strength of the material when compared to the samples processed under fully dense conditions. Meanwhile, larger pores from lack-of-fusion voids (200–500 µm) can lead to considerable pore structure irregularities, resulting in a pronounced reduction in the ultimate tensile strength of the material. Equiaxed grains in the horizontal direction, which are more isotropic and have a random orientation, tend to have lower porosity than columnar grains in the vertical direction. This can be due to more uniform solidification and better bonding between layers in the equiaxed microstructure [33].

From a tribological performance perspective, Hertzian analysis was utilized to calculate the contact area between the Ti6242 specimens and the ball counter face to understand the impact of the pore size on wear mechanisms. According to Hertzian theory, the contact radius, "*a*" can be calculated using the Eqs. (1) and (2) [34]:

$$a = \sqrt[3]{\frac{3FR}{4E^*}} \tag{1}$$

$$\frac{1}{E^*} = \frac{1-\nu_1^2}{E_1} + \frac{1-\nu_2^2}{E_2} \tag{2}$$

where F is the load on the contact area (= 5 N), R is the radius of the alumina ball (= 5 mm), and E^* is the reduced elastic modulus. $E_1 \approx 200$ GPa and $E_2 \approx 380$ GPa for the Ti6242 sample and Al_2O_3 ball, respectively. $\nu_1 = 0.32$ and $\nu_1 = 0.21$ for the Poisson's ratio of the specimen and the counter-face, respectively. Based on the current analysis, the contact diameter under this load is twice the contact radius, measuring approximately 100 µm. This value is smaller than the pore sizes in horizontal or vertical directions, which range from 200 to 500 µm. While the relatively small contact area suggests that direct interaction between the counterface and large surface pores may be limited, it should be noted that subsurface pores can still influence the local stress distribution and deformation behavior during sliding. Nevertheless, under the present testing conditions, no clear evidence of pore-induced wear damage was observed. These findings are further corroborated by the work of Islam et al. [34], which explored the wear mechanisms associated with both small and large pores.

3.2 Surface analysis

Figure 5a displays the mean surface roughness (*Ra*) of Ti6242 in both horizontal and vertical directions in their as-built states and after grinding. The as-built vertical orientation exhibits approximately 84.5% higher roughness

compared to the horizontal direction. Nevertheless, after grinding with SiC papers, the surface roughness was reduced to less than 0.4 µm, regardless of print direction.

SEM images in Fig. 5b–d depict the surface morphology of the Ti6242 alloy before and after grinding. The horizontal surface (Fig. 5b) exhibits distinct parallel lines, indicative of the layer-by-layer construction of the components during the EB-PBF process. Conversely, the vertical surface (Fig. 5c) exhibits a rougher surface, with irregularities like bumps and partially melted powder particles dispersed across the surface. After the grinding process, a smooth surface with minimal asperities can be achieved, as illustrated in Fig. 5d.

The layered nature of AM parts induces the stair-stepping effect on the surface topography, contributing to high roughness. This effect predominantly depends on the printing directions [35, 36]. When the electron beam irradiates the preset powder bed, it generates a molten pool with varying surface tension due to the different volumes of elements present [37]. In the case of vertical samples, the absence of a remelting process in the regions of stair steps means that the effect of the particle concentration on the surface of the previous layer cannot be omitted. Conversely, the surface of the horizontal sample benefits from the remelting phenomenon between neighbouring layers, resulting in a finer surface finish.

3.3 Microstructural analysis

Figure 6a presents the XRD patterns of the Ti6242 alloy printed in different build orientations. The XRD results reveal a consistent presence of α (hcp) and β (bcc) phases in both directions. The α phase, stabilized mainly by Al and Sn, shows higher peak intensities in the horizontally built samples, where faster heat dissipation due to larger surface exposure may promote α-phase formation [38] In contrast, vertically built structures retain heat longer, which can result in a different phase distribution, impacting the material's performance. A predominance of the α phase in the horizontal direction typically enhances the hardness, particularly at the top surface.

Dislocation density can be determined through various techniques, such as Transmission Electron Microscopy (TEM) [39], indentation [40], and XRD [41]. In this study, we employed the XRD method, specifically utilizing the well-known Williamson-Hall approach [42] to assess dislocation density. According to this method, the broadening

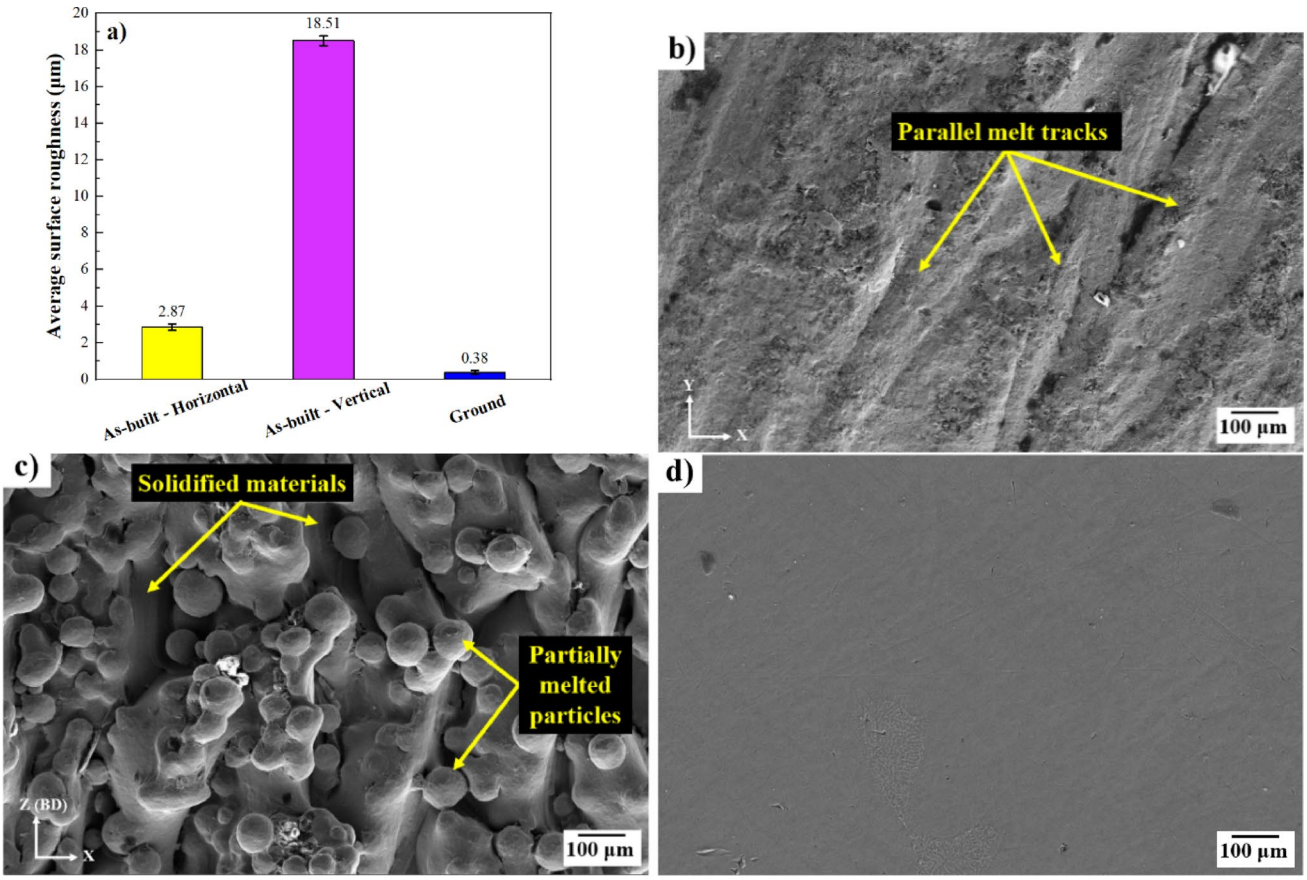


Fig. 5 **a** Average surface roughness of the as-built and ground Ti6242. SEM surface analysis of as-built Ti6242 in the **b** horizontal direction, and **c** vertical direction, and **d** Ti6242 sample after grinding

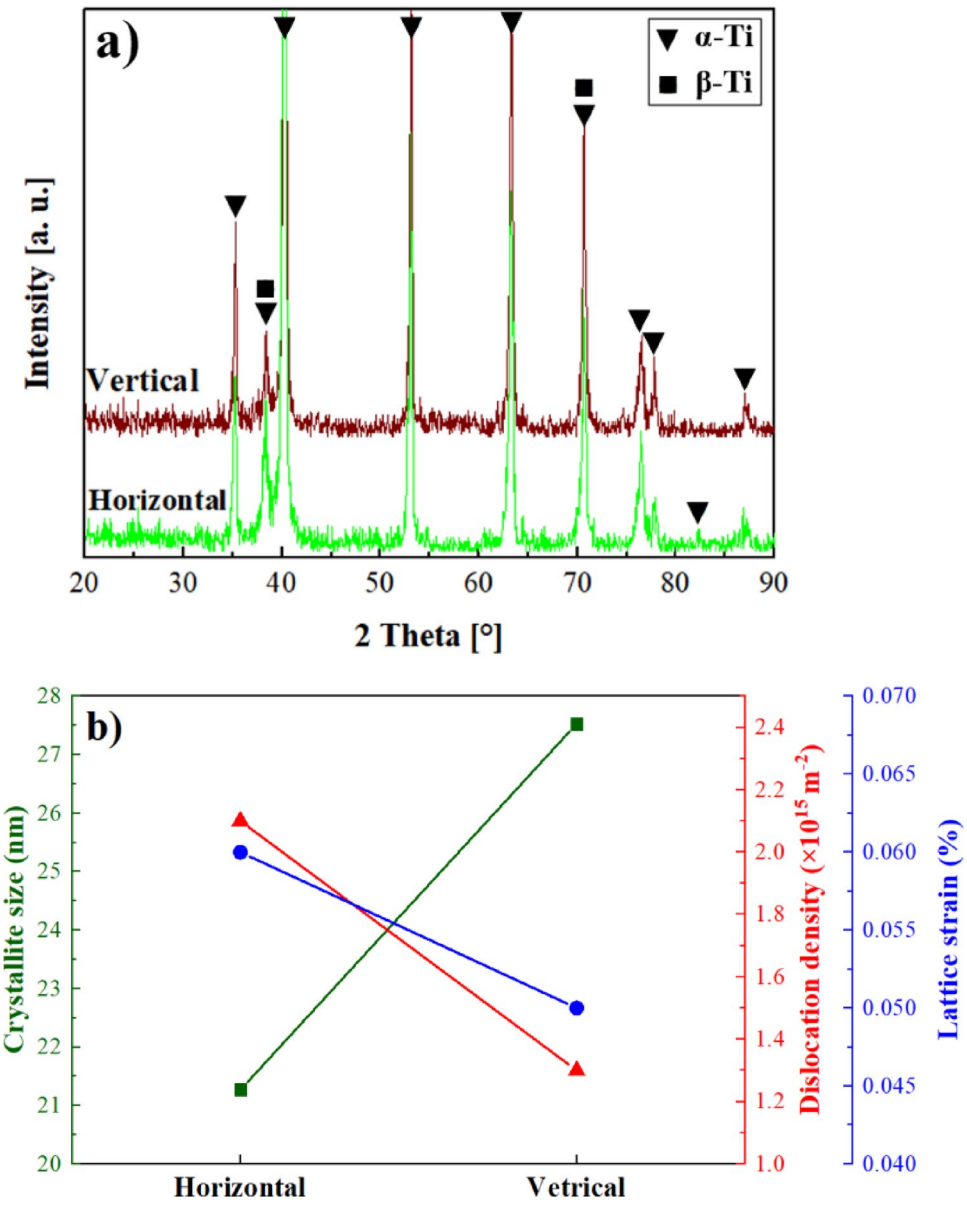


Fig. 6 **a** XRD patterns of the Ti6242 samples printed in horizontal and vertical directions. **b** The relationship between the build orientation and the variations in average crystallite size (Black square), dislocation density (Black up pointing triangle), and lattice strain (Black circle)

of the XRD peaks, compared to those of an ideal crystalline lattice, is influenced by both the crystallite size and the lattice strain. Equations (3, 4, 5) represent the calculations for dislocation density (ρ), lattice strain (ε), and crystallite size (D) [43]:

$$D = \frac{k\lambda}{\beta_{hkl}\cos\theta_{hkl}} \tag{3}$$

$$\rho = \frac{1}{D^2} \tag{4}$$

$$\epsilon = \frac{\beta}{4tan\theta_{hkl}} \tag{5}$$

where k, λ, β_{hkl}, θ_{hkl} are a constant≈0.9, X-ray wavelength (0.154 nm), full width at half maximum intensity, and the Bragg's angle at each peak. The lattice parameters (D, ρ, and ε) were determined by averaging the values obtained from each peak and the results are shown in Fig. 6b.

The mechanical properties of the EB-PBF-Ti6242 sample, including yield strength and hardness, are closely linked to the formation and movement of dislocations. In this study, the calculated dislocation density for the horizontal and vertical samples is 2.1×10^{15} m^{-2} and 1.3×10^{15} m^{-2}, respectively. Various theories have been suggested to explain dislocation formation in AM components [44]. For instance, the elements segregation at the cell walls plays a role in the dislocation formation, as a pronounced gradient in solute concentration at these boundaries can result in

strain hardening. Consequently, dislocations may develop to alleviate this strain energy. However, it has been noted that the localized stress and segregation can only generate a maximum dislocation density of around 10^{13} m^{-2} [45]. For Ti6242 alloys, the observed dislocation density is found to be 100 to 200 times greater, indicating that localized segregation at the cell boundaries alone cannot fully explain the observed dislocation generation. Residual stresses are thought to be another important factor contributing to the elevated dislocation density. Such stresses are common in additive manufactured metals due to the thermal histories associated with AM, which result in solidification shrinkage and thermal expansion, leading to dislocation accumulation [46].

In this study, the larger printing surface of the horizontal samples per layer, which results in higher cooling rates and residual stress compared to vertical samples, produces more dislocation density. Consequently, faster cooling in the horizontal orientation can lead to smaller crystallite sizes, in contrast to the characteristics observed in the vertical samples. Supporting this discussion, the XRD results shown in Fig. 6 indicate that lattice strain is greater in the horizontal samples than in their vertical counterparts.

The low and high-magnification OM images of the Ti6242 microstructure are provided in the Fig. 7a-e. The development of epitaxial grain growth occurs due to the sharp thermal gradient between the start plate and the melt pool surface subjected to the electron beam. This process results in the development of elongated columnar prior β grains in the build direction (normal to the powder bed) (Fig. 7d). Meanwhile, the cross-sectional view of these grains, exhibiting an equiaxed structure (parallel to the powder bed), is illustrated in Fig. 7a. It is generally believed that local variations in heat transfer may cause a misalignment between the growth direction and the build direction, resulting in the growth of columnar dendrites that are not always perfectly parallel to the direction of construction [24].

In high-magnification images, a non-uniform microstructure featuring a basketweave pattern of α + β phases is observed in both specimens. This can be attributed to recurrent heating cycles induced by the upper sintered layers and the thermal influence from the powder bed during the EB-PBF process. These conditions prompt a transformation of the α' martensitic phases into the α phase within the existing β grains. Consequently, a primary Widmanstätten microstructure with a basketweave structure takes shape, accompanied by the presence of α colonies near the boundaries of the β grains [47]. It is well documented that the complex thermal history during the EB-PBF process could result in the following sequence of phase transformations during the melting and cooling of the Ti alloys [48].

$$S_{(powder)} \rightarrow L_{(melt)} \rightarrow \beta_{prior} \rightarrow \alpha' + \alpha_{primary} + \beta_{retained} \rightarrow \alpha + \beta$$

The findings are further supported by the SEM image shown in Fig. 7c, f. As mentioned eralier, in EB-PBF process, the cooling rate is faster in the horizontal orientation due to the heat dissipation through the layers, resulting in quicker cooling across each layer. This leads to the formation of thinner and finer α laths (dark regions) and narrower β phase (bright regions) in the microstructure. In SEM image of the horizontal sample (Fig. 7c), the refined α lath colonies aligned parallel to the build layers can be observed, with small thickness of α lath and β phase. In contrast, in the vertical orientation (Fig. 7f), the slower cooling rate allows for the growth of thicker and shorter α laths and β phase, where the α and β phases have had more time to develop into larger and more defined regions.

To gain deeper insight into the microstructural characteristics of the specimens, EBSD analysis was performed for horizontal (Fig. 8a, c) and vertical (Fig. 8b, d) samples. The results reveal the presence of large, discernible regions or colonies composed of multiple α lamellae with varying orientations, as indicated by the diverse color contrast in the Inverse pole figure (IPF) maps obtained along the build direction. The orientation of the α lamellae is primarily governed by two factors: the epitaxial growth of prior columnar β grains during the EB-PBF process, and the crystallographic nature of the phase transformation.

The IPF maps did not reveal any pronounced crystallographic texture along the build direction, suggesting a rather random orientation of α lamellae. In HCP metals such as Ti6242, the < 10–10 > direction is typically associated with the fastest crystal growth due to its alignment within the basal plane [49]. This lack of texture is attributed to the transformation mechanism from β to α (or α′), where the crystallographic information from the parent β phase, often exhibiting a strong < 100 > fiber texture along the build direction, is not always retained. This is especially true when the transformation results in acicular or basketweave morphologies, which promote a randomized texture in the final microstructure [50].

Moreover, grain morphology was quantified by fitting a best-fit ellipse to each EBSD-defined grain and extracting its principal axes, the major axis (L_1) and minor axis (L_2). The shape aspect ratio was defined as $\varphi = L_2/L_1$; grains with $\varphi \leq 0.33$ ($\approx$ 1:3 minor-to-major) were classified as columnar, whereas grains with $\varphi > 0.33$ were classified as equiaxed [51]. Figure 8 compares the influence of build orientation on grain shape and on the columnar/equiaxed partition for horizontally and vertically fabricated specimens, and Fig. 8c, d reports the area-fraction distributions across aspect-ratio bins. Horizontally built samples contained 60.7% columnar

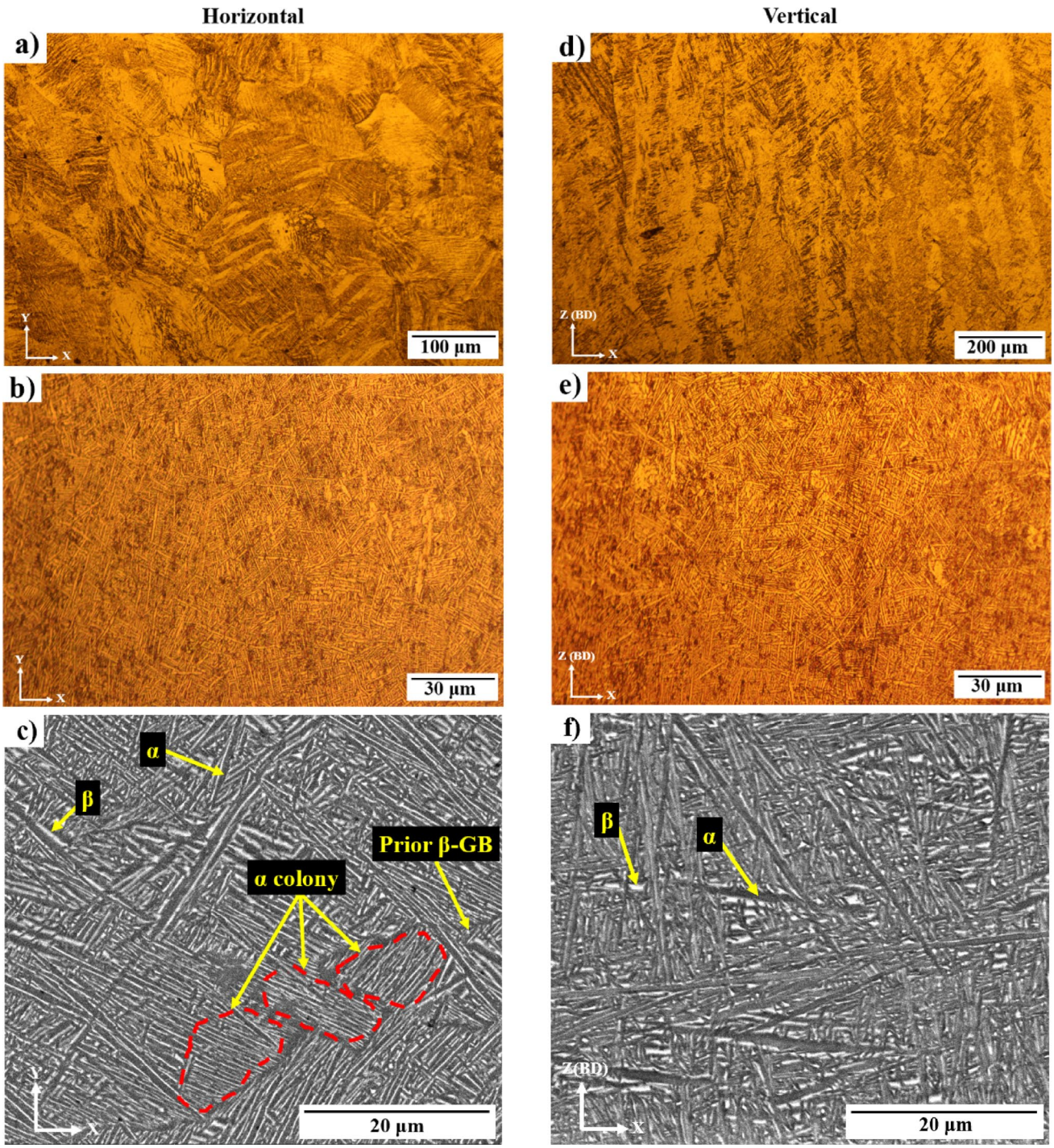


Fig. 7 OM Microstructure of the (**a**, **b**) horizontally and (**d**, **e**) vertically built Ti6242 specimens. SEM Microstructure of the (**c**) horizontally and (**f**) vertically built Ti6242 specimens

grains, while vertically built samples contained 66.4% columnar grains. This difference is attributed to orientation-dependent solidification conditions, namely changes in cooling rate, thermal gradient, and solidification (interface) velocity that arise from altering the build direction.

The Schmid factor (SF) is defined as $\mathrm{SF} = \cos\phi\cos\lambda$, the geometric factor giving the resolved shear stress on a slip system relative to the applied uniaxial stress ($0 \leq \mathrm{SF} \leq 0.5$). SF mapping performed for HCP slip systems; basal $\{0001\}\langle 11\text{–}20\rangle$, prismatic $\{10\text{–}10\}\langle 11\text{–}20\rangle$, pyramidal-I $\{10\text{–}11\}\langle 11\text{–}23\rangle$ (c+a), and pyramidal-II

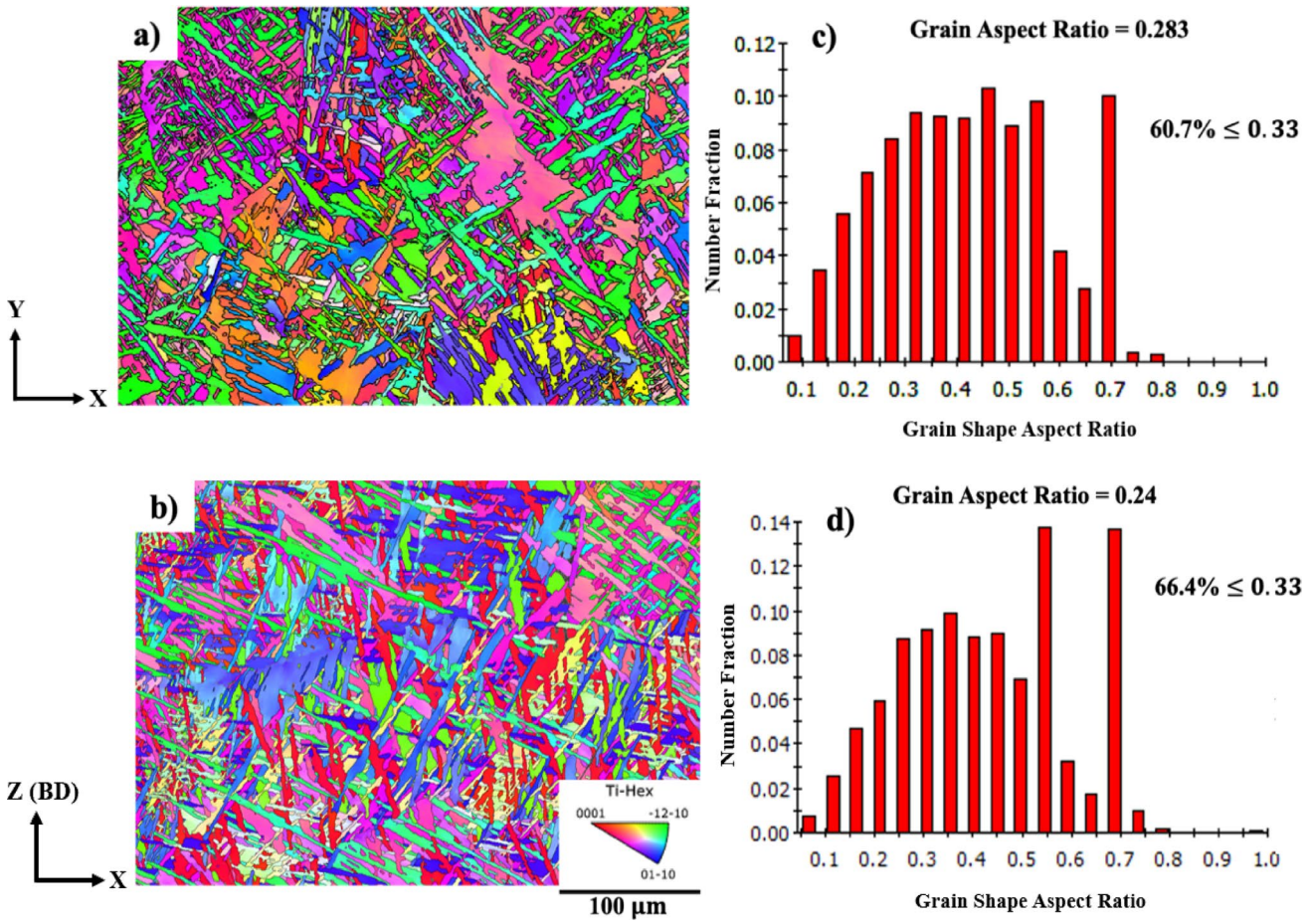


Fig. 8 Inverse pole figure (IPF) maps and grain aspect ratio distribution of the Ti6242 specimens fabricated in two different build direction: (**a**, **c**) Horizontally, and (**b**, **d**) Vertically

{11–22}⟨11–23⟩ (c + a); reveals a clear orientation dependence between horizontal (left column) and vertical (right column) builds, as illustrated in Fig. 9. It can be seen that, relative to the horizontal specimen, the vertical build shows higher ⟨SF⟩ for basal (0.308→0.342), prismatic (0.310→0.331), and pyramidal-I (0.393→0.407), while pyramidal-II remains essentially unchanged (0.434 vs. 0.433). The right-shifted histograms in the vertical condition indicate a larger fraction of grains favorably oriented for these systems with respect to the loading axis used in the SF calculation. Geometrically, the vertical build is therefore more permissive for activation of basal/prismatic and first-order pyramidal (c + a) slip, whereas any differences in hardness/yield between orientations must arise from variations in Critical Resolved Shear Stress (CRSS) and microstructural strengthening rather than SF geometry alone.

To place these observations in context, previous studies on AM-HCP titanium alloys have reported similar orientation-dependent SF behavior. Yang et al. [52] showed that vertically fabricated Ti6Al4V samples exhibited right-shifted SF distributions for basal and prismatic ⟨a⟩ slip, which correlated with higher ductility and reduced tensile anisotropy compared with horizontally built specimens. This was attributed to the preferential inclination of the α-phase c-axes toward the loading direction, thereby increasing the resolved shear stress on the dominant slip systems. Likewise, Dharmendra et al. [53] employed EBSD-based SF mapping and demonstrated that AM-induced texture heterogeneity causes systematic differences in slip geometry between horizontal and vertical builds. Their vertical specimens displayed higher average SFs and a narrower population of low-SF grains, suggesting a more uniform and favorable configuration for slip activation under applied load.

More recent high-resolution EBSD investigations on L-PBF-Ti6242 by Kaushik et al. [54] further emphasized that SF geometry alone cannot fully explain mechanical anisotropy. Although a large fraction of grains in the as-built condition possessed SF > 0.4 for pyramidal ⟨c + a⟩ systems, the relatively high CRSS associated with this mode, together with microstructural barriers such as α/β interfaces and dislocation substructures, limited actual slip

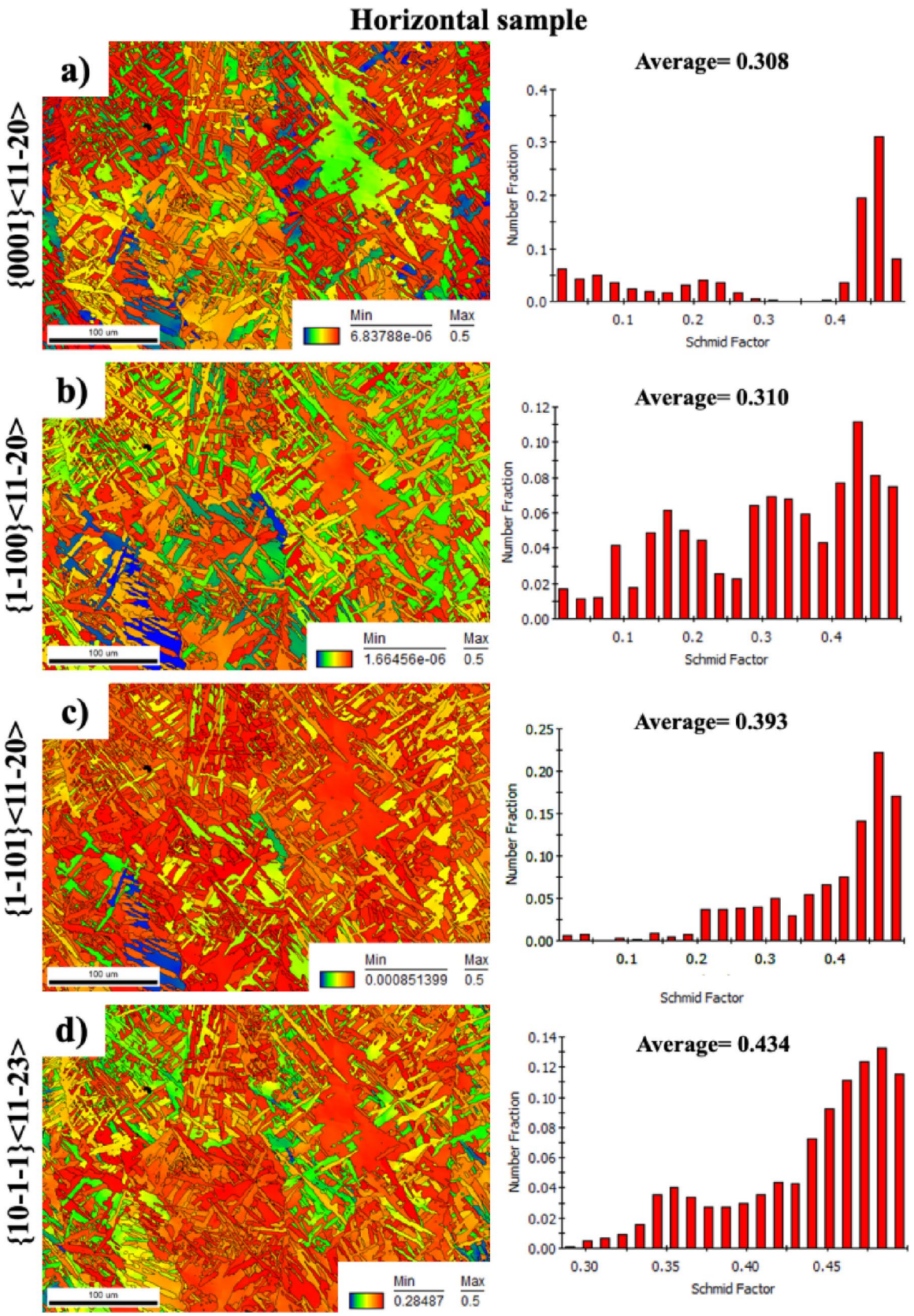

Horizontal sample
a)
{0001}<11-20>
Min
6.83788e-06
Max
0.5
100 um
Average= 0.308
Number Fraction
Schmid Factor
b)
{1-100}<11-20>
Min
1.66456e-06
Max
0.5
100 um
Average= 0.310
Number Fraction
Schmid Factor
c)
{1-101}<11-20>
Min
0.000851399
Max
0.5
100 um
Average= 0.393
Number Fraction
Schmid Factor
d)
{10-1-1}<11-23>
Min
0.28487
Max
0.5
100 um
Average= 0.434
Number Fraction
Schmid Factor

Fig. 9 Schmid factor maps and distributions for HCP slip systems under horizontal and vertical builds: (**a**, **e**) basal $\{0001\}?11\bar{2}0?$; (**b**, **f**) prismatic $\left\{10\bar{1}0\right\}?11\bar{2}0?$; (**c**, **g**) pyramidal-I ($\langle c+a\rangle$) $\left\{10\bar{1}1\right\}?11\bar{2}3?$; (**d**, **h**) pyramidal-II ($\langle c+a\rangle$) $\left\{11\bar{2}2\right\}?11\bar{2}3?$. Mean SF (horizontal → vertical): 0.308 → 0.342, 0.310 → 0.331, 0.393 → 0.407, and 0.434 → 0.433, respectively

activity. Consequently, geometric favorability must be interpreted alongside microstructural parameters (like lath thickness, colony size, and dislocation density) that modulate the effective CRSS.

The present results are therefore consistent with this mechanistic framework: In the present study, while vertically built EB-PBF–Ti6242 samples exhibit higher mean SFs and a greater fraction of favorably oriented grains for basal and prismatic systems, the modest mechanical differences between orientations are primarily governed by microstructural strengthening and slip resistance rather than Schmid geometry alone. The increased ⟨SF⟩ observed in the vertical condition thus signifies a more permissive crystallographic configuration for slip initiation, yet the absence of significant softening confirms that deformation behavior remains controlled by the intrinsic CRSS hierarchy and α/β morphology characteristic of EB-PBF-processed Ti6242.

3.4 Mechanical properties

Figure 10a compares the microhardness of the Ti6242 specimens fabricated horizontally and vertically. The microhardness of the horizontal specimen aligns with that of the vertical one, exhibiting a slight increase of approximately 2%. The microhardness contour maps shown in Fig. 10b, c further indicate that the hardness distribution is relatively uniform across both specimens, with only minor local variations. The loading-unloading curves of the Ti6242 samples are presented in Fig. 10d. The indentation depth of the sample with the vertical orientation was slightly greater than the horizontal plane. The elastic modulus and nano hardness values are reported in Table 2. The nano hardness is rarely independent of the elastic modulus. A 6% increase in nano hardness and elastic modulus was observed by changing the build direction from the vertical direction to the horizontal.

The evaluation of nano hardness relies on the projected area at the maximum load, which is usually smaller than the residual projected area used in microhardness testing, leading to higher hardness values than microhardness [55]. A partial increase in hardness and elastic modulus observed in the horizontal sample compared to the vertical one can be attributed to some microstructural and geometrical factors. Firstly, as seen in Fig. 6a, XRD analysis indicated a higher presence of the α phase in the horizontally oriented sample. Given that the α phase generally exhibits greater hardness than the β phase [56], this contributes to the overall hardness enhancement. Additionally, the EBSD results indicated lower average Schmid factor values for the horizontal condition, suggesting that fewer grains were favorably oriented for slip activation under applied loading. The lower Schmid factor implies a greater resistance to dislocation motion, leading to higher hardness and yield strength. The finer α-lath morphology and the more randomized orientation of α lamellae observed in the horizontally built samples also enhance microstructural strengthening by impeding slip transmission across grain and phase boundaries. Furthermore, larger pores in the vertical direction (Fig. 4) can act as stress concentration points, reducing the mechanical properties of the material. Smaller pores in the horizontal direction, while still affecting the material's properties, might have a lower impact on the hardness and elastic modulus compared to their larger counterparts [30, 57]. When the porosity content and size surpass a critical threshold, internal defects predominantly negatively affect the mechanical properties by diminishing the effective load-bearing cross-section during load application. Consequently, there is a pronounced inverse correlation between hardness and mechanical properties with porosity size in such a way that the larger pores may contribute to the notch effect, ultimately reducing both static and dynamic strength, particularly when their geometry is irregular and features sharp edges which are the characterisitcs of the lack of fusion (LOF) porosity [27, 58].

3.5 Friction and wear resistance analysis

Figure 11 presents the coefficient of friction (COF) variation with sliding time for the Ti6242 samples. It can be seen the COF of both horizontally and vertically oriented specimens at room temperature exhibits an upward trend at the running-in period with relatively high fluctuation and then goes into a steady stage (Fig. 11a). Indeed, during the initial phases, surface asperities increased the frictional resistance and consequently resulted in an elevation in the COF. As the asperities progressively smoothed out, the COF eventually stabilized at around 0.5.

In Fig. 11b, at 250 °C, the COF continuously increased during the running-in period, reaching a steady value of ~ 0.58. The initial increase can be attributed to the elimination of oxide layers, which weaken the metal-to-metal adhesion between contact surfaces. Removing these layers increases metal-to-metal and/or metal-to-wear particle contact, thereby enhancing the adhesive and ploughing components of the COF [59]. Once the surface layers were entirely eliminated and a balance was achieved between the generation and expulsion of wear debris, the COF stabilized constantly.

At 450 °C, the COF change was the same as at 250 °C, with the difference that the COF decreased rapidly in the

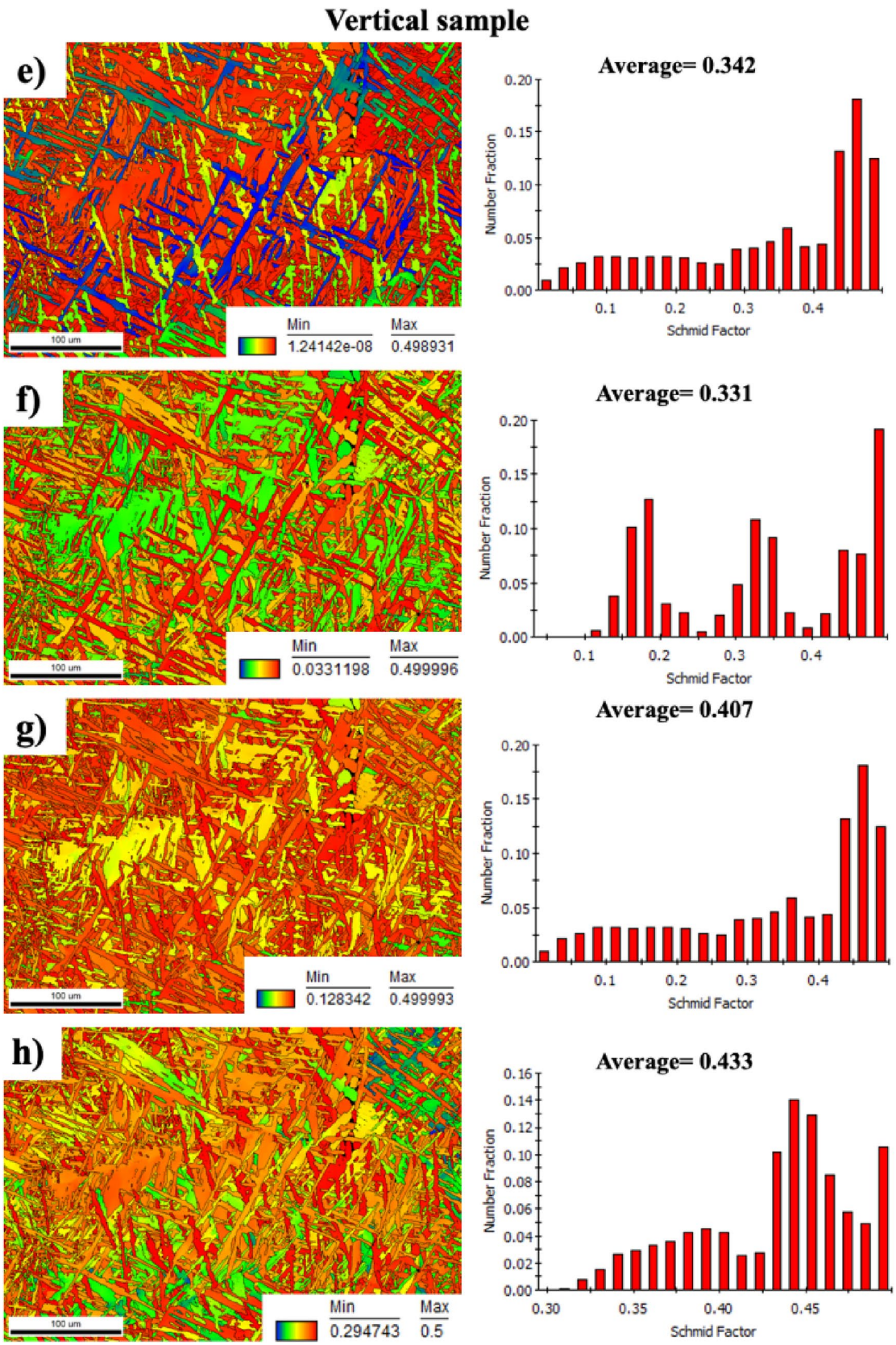


Fig. 9 (continued)

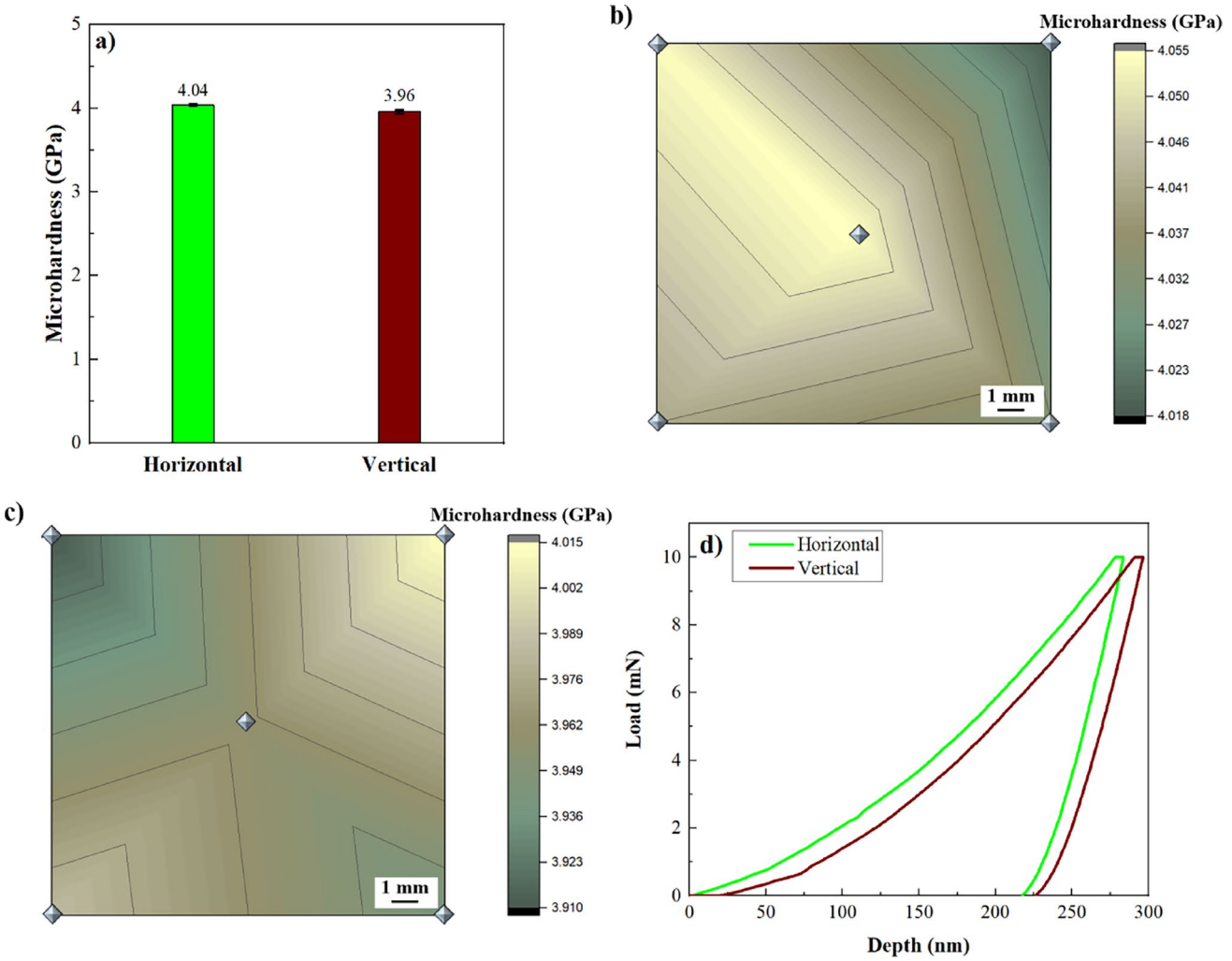


Fig. 10 **a** Microhardness values of the Ti6242 samples. Contour maps relative to the Vickers hardness measurements for **b** horizontally and **c** vertically oriented samples (The diamond-shaped marks indicate the Vickers indentation footprints used for the microhardness contour mapping). **d** Nanoindentation loading-unloading curves for the samples in different building angles

Table 2 Nano hardness and elastic modulus of the horizontally and vertically oriented Ti6242 samples

	Nanohardness (GPa)	Elastic modulus (GPa)
Horizontal	6.17±0.01	213.57±9.15
Vertical	5.80±0.03	199.47±7.54

initial stages and then increased until it reached a steady period (Fig. 11c). Moreover, the COF in the constant region (~0.51) was lower than at 250 °C and similar to the COF of the samples at room temperature.

Two critical points are extracted from the COF graphs:

Firstly, the COF of the samples made in both horizontal and vertical directions closely resembled each other at 25 °C and 450 °C, and the highest COF was obtained under 250 °C. Similar behavior has been reported for Ti alloys by Wang et al. [7] and Li et al. [60], where unstable or partially developed oxide layers formed at 200–300 °C led to enhanced adhesive and three-body abrasive wear. At these temperatures, the protective tribo-oxide film is repeatedly formed and ruptured, resulting in severe debris generation and metal-to-counterpart contact. At higher temperatures (≥ 400 °C), however, a stable and dense TiO_2-based tribo-layer can develop.

Secondly, the horizontal and vertical samples showed similar tribological behaviour at each temperature, confirming the isotropic wear resistance for Ti6242 samples produced via the EB-PBF process. Similar observations have been reported in previous studies investigating the influence of build orientation on the mechanical and fatigue properties of additively manufactured metals. Jeffs et al. [61] reported that although vertically oriented EB-PBF-Ti6Al4V samples exhibited slightly higher impact energy than horizontally built ones, the difference was marginal when optimized process parameters were applied, indicating that the EB-PBF process can yield near-isotropic mechanical behavior. Similarly, Wood et al. [62] demonstrated that horizontally

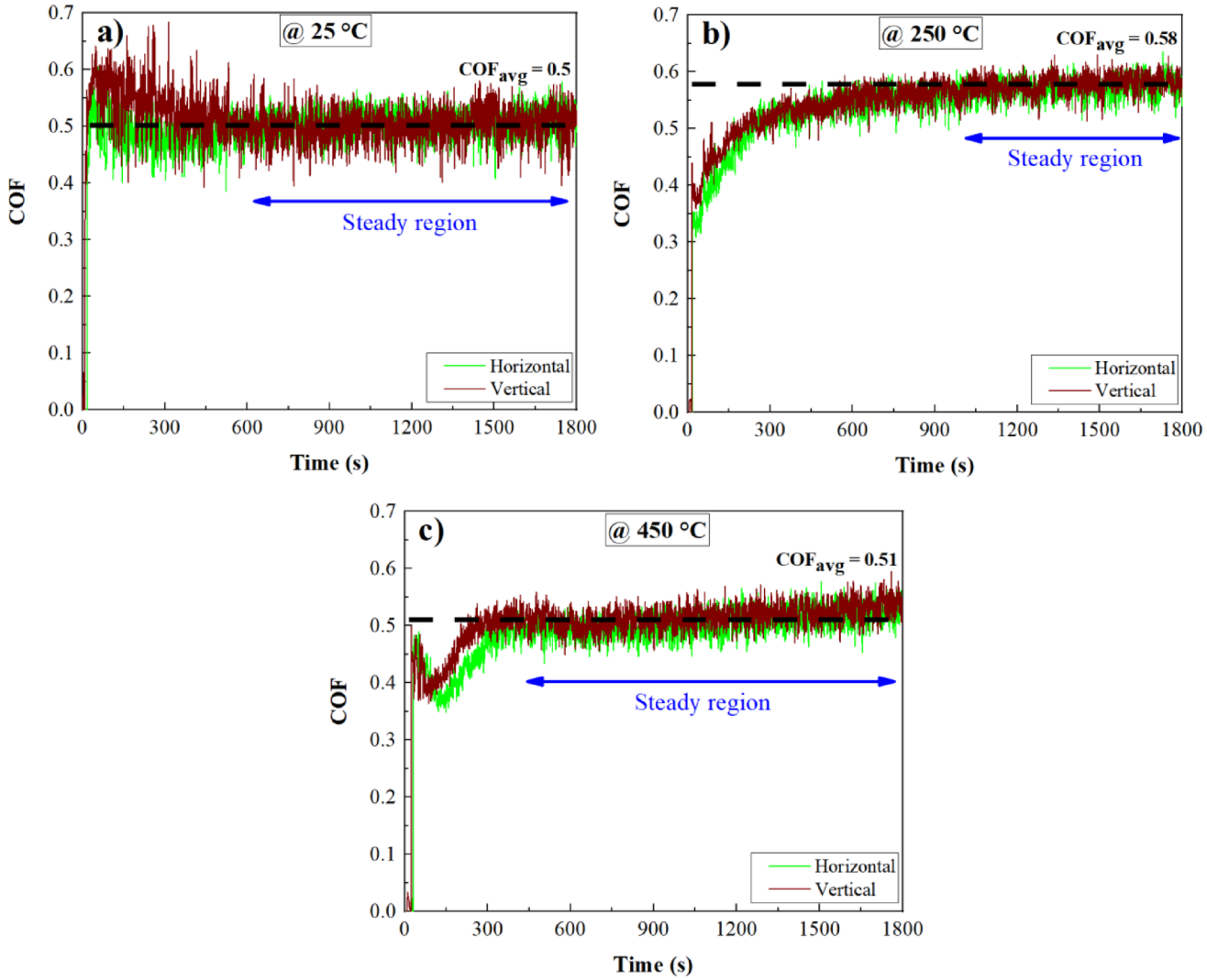


Fig. 11 The COF of horizontally and vertically built Ti6242 alloy at different temperatures

built and machined L-PBF-316 L stainless-steel specimens displayed fatigue strengths comparable to vertically built counterparts once surface defects were minimized through post-processing. These studies collectively suggest that when the layer-by-layer thermal history produces a uniform α-lath or grain morphology, and when post-fabrication treatments effectively mitigate defect-driven anisotropy, the influence of build direction on mechanical and surface-related properties can be considerably reduced.

Figure 12 illustrates the wear depth profiles and the calculated wear volumes of the Ti6242 specimens after the sliding tests. The wear volume ($V = 2\pi rS$) was determined according to Ref [63], where r denotes the wear track radius (10 mm) and S corresponds to the cross-sectional area of the wear groove derived from the wear depth profiles. The value of S was obtained using OriginPro software. To ensure the reliability of the measurements, the cross-sectional area for each sample was calculated as the average of three independent wear profiles taken at different positions along the wear track.

The results show that both orientations exhibited the highest wear volume at room temperature, which was approximately 10% higher than that observed at 450 °C. In contrast, the lowest material loss was recorded at 450 °C. This trend is generally consistent with the friction behavior observed during the tests. Overall, the difference in wear volume between the horizontally and vertically built samples remained negligible at all tested temperatures, indicating similar wear performance for both build orientations.

The temperature-dependent tribological behavior of Ti6242 can be explained by the progressive development of surface oxidation during sliding. At room temperature, the native oxide layer is thin and unstable, leading to repeated metal–ceramic contact, which results in the largest wear volume and noticeable fluctuations in the COF. At 250 °C, partial oxidation promotes the formation of a thin and unstable oxide layer. The

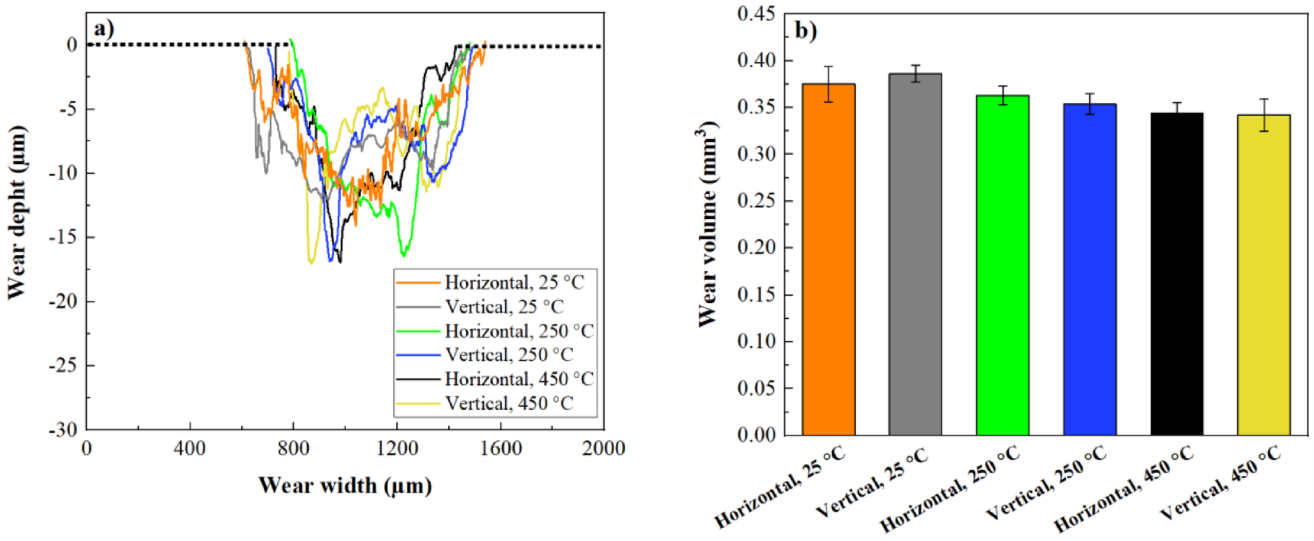


Fig. 12 Wear depth profiles and calculated wear volumes of the Ti6242 specimens

repeated formation and fragmentation of this layer generates oxide debris within the contact, which increases the interfacial shear resistance and surface roughness, and results in a slightly higher COF. When the temperature increases to 450 °C, a more stable and continuous TiO_2-based tribolayer can form on the sliding surface, acting as a protective barrier that reduces material removal and leads to the lowest wear volume.

A thorough examination of the worn surfaces was conducted using SEM to gain deeper insights into the wear mechanisms, as depicted in Fig. 13. Secondary electron (SE) and backscattered electron (BSE) imaging were employed to observe the surface morphology and ascertain the phase distribution, respectively. Additionally, EDS analysis was carried out on the wear tracks, and the results of three main elements (Ti, O, and Al) are presented in Table 3 (Each of the other elements, including Si, Zr, Mo, and Sn, were less than 1 wt%). The findings from the SEM images of wear tracks corroborated the patterns observed in the friction analysis. The degree of degradation and wear mechanisms across different build orientations exhibited notable similarities. Numerous regular abrasion furrows are observable on the worn tracks of the Ti6242 alloys. These furrows stand as distinctive features attributed to the ploughing effect.

Given that the hardness of the Al_2O_3 ball dramatically surpasses that of the titanium alloy, the alumina's projections become embedded within the titanium surface. Consequently, during sliding, these projections displace the plastic flow of the Ti6242 alloy, ultimately sculpting grooves. The combined effects of ploughing and localized delamination lead to surface spalling and plastic deformation occurring on the surface. The recurrent "work hardening-delamination" process could be the fundamental cause of the fluctuations observed in COF curves [64, 65]. Upon closer examination, it becomes apparent that samples displayed wear debris on their surfaces. The likelihood of three-body abrasive wear arises from the presence of the detached small fragments that were re-crushed by the alumina ball [66].

Based on the BSE images of the worn surfaces, the darkened region extends from room temperature to 450 °C. The EDS analysis (Table 3) of the selected areas revealed a relatively elevated oxygen content, suggesting the surface oxidation at 250 °C and 450 °C, which suggests the occurrence of oxidative wear during the tests. Ti and O elements observed on the worn surfaces at elevated temperatures indicate the possible formation of titanium oxide films, known for their lubricious nature and ability to undergo elastoplastic deformation under normal loads and shear stresses [67]. The improved COF at 450 °C, compared to 250 °C, can be attributed to the higher oxygen concentration, leading to the increased formation of titanium oxide with self-lubricating properties. It should be emphasized that the formation of TiO_2 is inferred from EDS data. Nevertheless, it is noteworthy that the strength and hardness of Ti alloys decrease at higher temperatures [68]. Consequently, the combined influence of these two effects results in no significant impact of temperature on the tribological behaviour of this alloy [60]. Hence, the COF of the sample is comparable at both room temperature and 450 °C. Another significant observation from EDS analysis is the elevated percentage of Al element at 250 °C compared to temperatures of 25 °C and 450 °C. This can be attributed to adhesive wear between the alumina ball and the titanium sample at this temperature.

The wear characteristics of AM components are influenced by several critical factors, including the composition of the material, which affects hardness and toughness (elastic modulus); microstructure, which varies depending on the AM process and impacts grain size and phase distribution; and surface finish, where smoother surfaces generally provide enhanced wear resistance [14, 69]. Since the grain morphology and hardness in the vertical and horizontal directions are

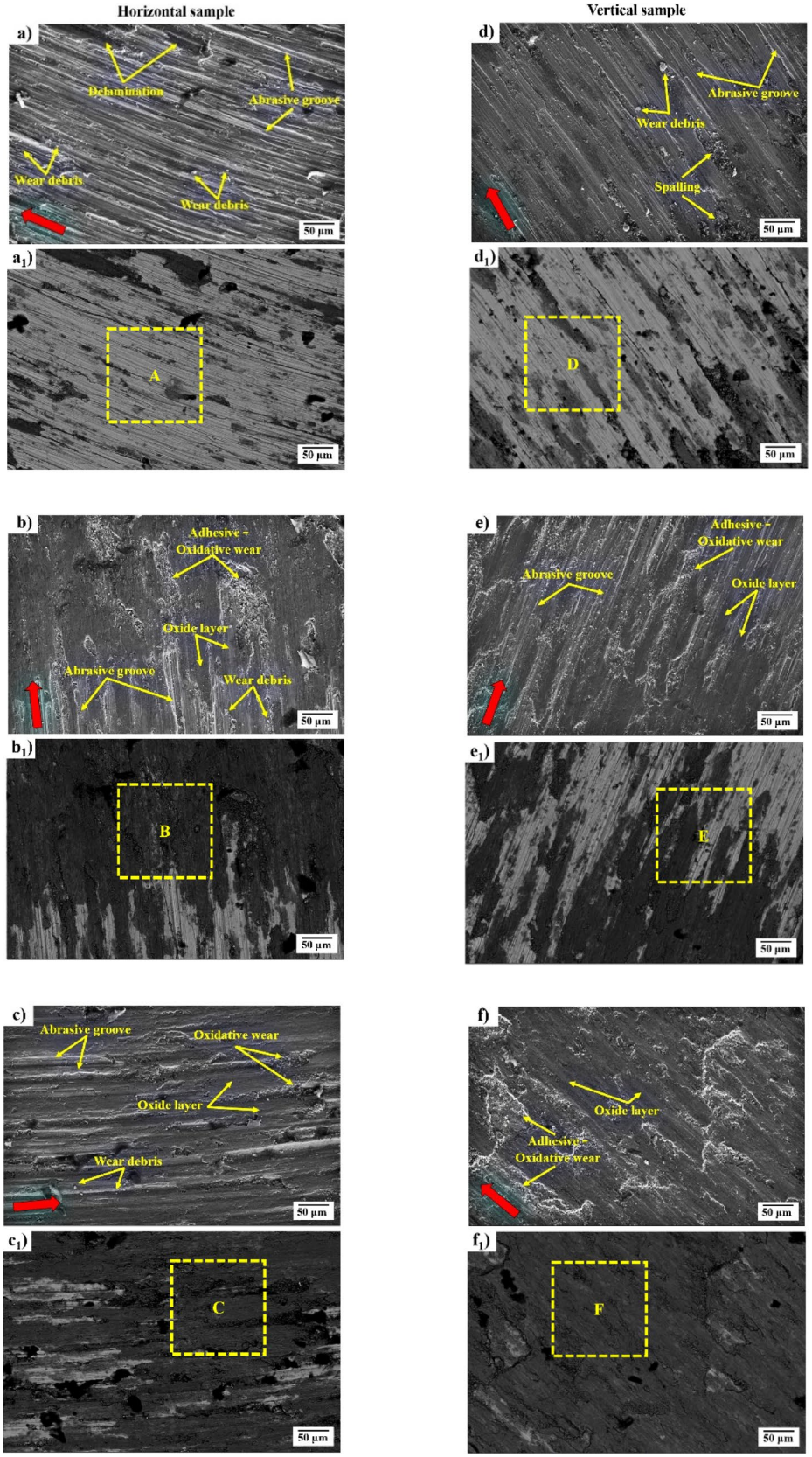


Fig. 13 SE and BSE images of wear surfaces for horizontal at (**a**, **a**$_1$) 25 °C, (**b**, **b**$_1$) 250 °C and (**c**, **c**$_1$) 450 °C, and for vertical Ti6242 samples at (**d**, **d**$_1$) 25 °C, (**e**, **e**$_1$) 250 °C and (**f**, **f**$_1$) 450° C. (sliding direction is shown with a red arrow)

Table 3 EDS analysis of the regions on the worn surfaces shown in Fig. 13

Region	Element (wt%)		
	Ti	O	Al
A	94.2	2.9	1.4
B	53.7	33.4	11.2
C	52.0	41.3	4.7
D	93.4	4.2	1.1
E	62.9	25.7	9.6
F	50.9	44.1	3.4

different, different wear resistance was also expected in these samples. However, no explicit correlation between build direction and tribological behaviour was observed. This unexpected performance can be due to some reasons. Firstly, as surface roughness is a critical factor in tribological behaviour, the striking similarity in the tribological performance of both samples can be attributed to their nearly identical surface roughness and topography achieved through grinding. During the wear test, a certain amount of energy is dissipated to activate the tribologically transformed structure (TTS) and generate wear debris. Notably, there exists an inverse relationship between surface roughness and cumulative dissipated energy. Since both samples exhibit the same average surface roughness, they also dissipate the same amount of energy [70]. This further supports the earlier discussion that appropriate post-processing can considerably reduce the influence of build direction on the surface-related properties of additively manufactured alloys. Secondly, the testing conditions, such as load, could play a role in minimizing the differences in wear behaviour between the two orientations. Subjected to a high load like 5 N, the elevated compressive stress leads to heavily worn grooves characterized by numerous parallel cracks. During sliding, two forces, including the tangential force (F_t) and the normal force (F_n), act on the cells, with the first one being responsible for initiating slipping [18]. The following simple relationships can be used to describe the F_t [71]:

$$F_t = \sum_{k \leqslant n} \tau_e A_e \tag{6}$$

$$F_t = \sum_{k \leqslant n} \tau_c A_c \tag{7}$$

where A_e and A_c are the cross-sectional areas of the equiaxed and columnar grains, respectively, and τ_e and τ_c are the shear stress of the equiaxed and columnar grains, respectively. Moreover, k and n indicate the couple of asperities and the total number of asperities pairs in contact, respectively. The equiaxed grains, having a smaller cross-sectional area compared to the columnar grains ($A_e < A_c$), experience more local shear stress under identical loading conditions ($\tau_e > \tau_c$). Consequently, certain segments of the equiaxed structures undergo destruction, signifying the onset of fracture dominance. This occurs when the shear stress within the equiaxed cells surpasses their ultimate strength while the shear stress within the columnar cells remains below this threshold. Therefore, despite the slightly higher hardness of the horizontal samples, the combined effects of local shear stress distribution and microstructural characteristics result in an almost isotropic wear behavior between the two orientations.

Another contributing factor to the nearly isotropic wear behavior of horizontal and vertical samples is the interplay between mechanical-geometrical and microstructural effects during sliding. To investigate the influence of the structural cell orientation and grain geometry on wear resistance, an initial analysis based on the sliding direction relative to the grain structure was performed. Figure 14 presents schematic diagrams depicting the wear resistance of different structural cells oriented in various directions to understand the mechanism better. Two extreme cases are analyzed for horizontal and vertical Ti6242 samples: one involves sliding parallel to the x-direction (S_{x-H} and S_{x-V}). In contrast, the other consists of sliding parallel to the y-direction (S_{y-H} and S_{y-V}). The wear resistance of the cell structures in other orientations falls between these two extremes. It should be noted that the xy plane defined for the wear test corresponds to the sliding surface and differs from the XY plane of the build orientation.

For the vertical sample with more columnar grains (Fig. 14a), nearly all the tangential force in the S_{x-V} direction facilitates slipping. In contrast, a significantly larger force is necessary to induce slipping in the S_{y-V} direction, as the force has only a small component aligned with the slipping direction. Consequently, the S_{y-V} direction exhibits greater resistance to slipping.

As illustrated in Fig. 14b, the equiaxed structure bends as the indenter moves, enhancing the tangential force component in the slipping direction. This leads to easy slipping occurring in both the S_{x-H} and S_{y-H} directions. These findings are in line with those reported by Yang et al. [18] on the wear anisotropy of AM components. This analysis indicates that sliding occurs more easily in horizontal samples along certain directions compared to vertical ones, due to the tangential force components and the grain morphology.

On the other hand, the vertically built specimens exhibit higher average Schmid factors for the dominant basal and prismatic slip systems, meaning that a larger fraction of grains are crystallographically oriented in a manner that promotes slip activation under the applied stress state. According to Schmid's law, plastic deformation in crystalline materials begins when the resolved shear stress acting on a slip system reaches the critical resolved shear stress (CRSS), and therefore grains with

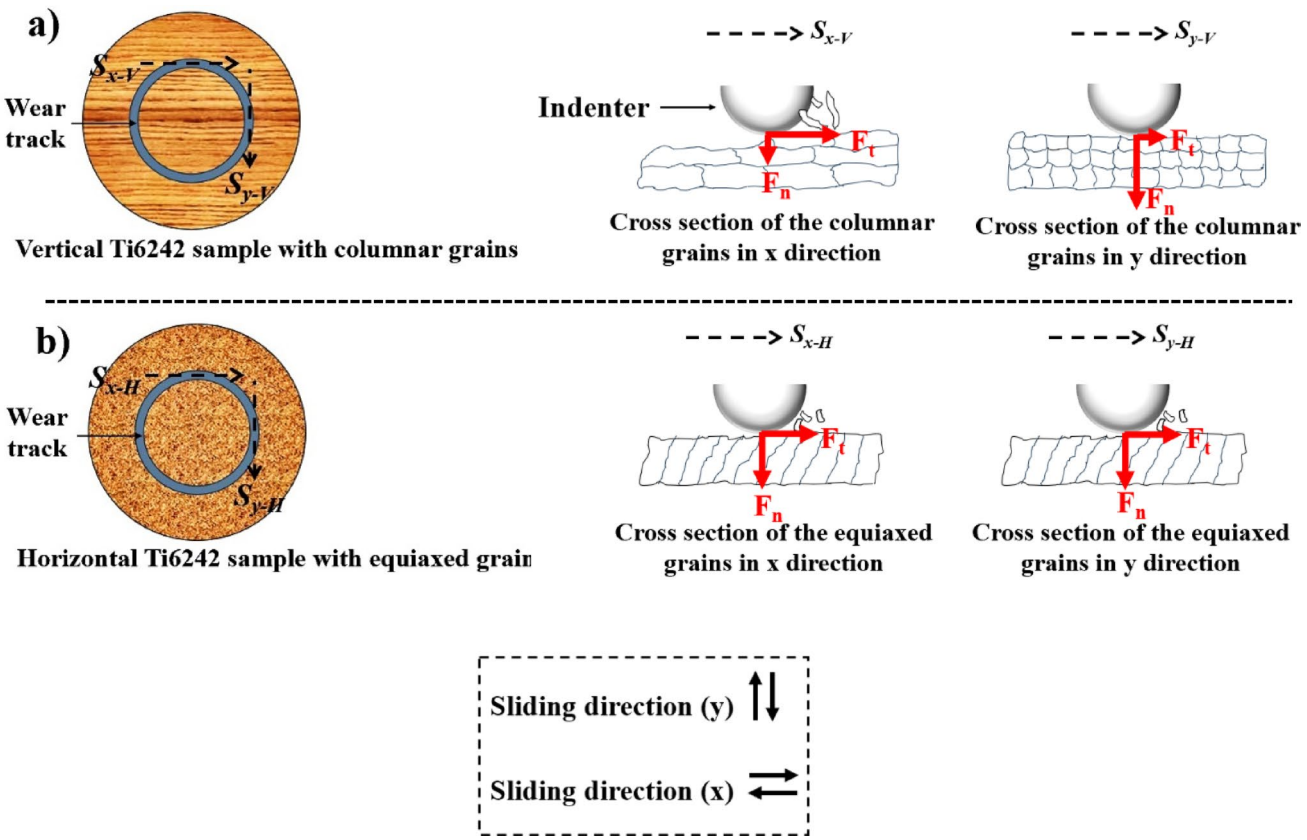


Fig. 14 The schematic diagram illustrates the various wear resistance mechanisms in cells oriented in different directions for **a** columnar and **b** equiaxed grains

higher Schmid factors can activate slip more readily under the same external load [72].

During sliding wear, the stress field beneath the contact is dominated by significant shear stresses generated by the tangential force component. In ductile metallic materials, such shear stresses are often accommodated through severe plastic deformation and dislocation motion beneath the contact interface rather than immediate fracture [73]. Consequently, grains that are favorably oriented for slip can plastically accommodate the imposed shear strain more efficiently, which reduces the likelihood of brittle asperity fracture and the formation of wear debris. Previous studies on sliding wear mechanisms have shown that surface asperities may either fracture to form wear particles or deform plastically depending on the local stress state and the material's ability to accommodate plastic strain [74, 75].

Therefore, the higher hardness of the horizontal specimens increases their resistance to deformation, whereas the higher Schmid factor of the vertical specimens promotes easier slip activation and plastic accommodation of shear stresses during sliding. These two microstructural characteristics represent different mechanisms controlling deformation within the subsurface region during wear. As a consequence, the effective shear response of both orientations becomes comparable under the applied sliding conditions. The combined effects of grain geometry and microstructural properties result in a similar effective subsurface response, leading to the nearly isotropic wear behavior observed in both horizontal and vertical samples.

4 Conclusions

In this work, Ti6242 alloys were successfully manufactured utilizing the EB-PBF process. Subsequently, the defect content, microstructure, mechanical, and wear characteristics of the samples produced in horizontal (0°) and vertical (90°) build directions were evaluated. The principal outcomes can be drawn as follows:

- EB-PBF processing of Ti6242 produced a non-uniform microstructure with a basketweave α+β phase pattern, featuring equiaxed grains in the XY plane and columnar grains in the XZ plane; vertically built specimens exhibited larger voids (~500 μm) due to distinct thermal histories compared to horizontal samples.
- EBSD results showed a predominantly random α-lamellar orientation without distinct texture, and

the vertical sample exhibited slightly higher average Schmid factors for basal and prismatic slip systems. This suggested a more favorable slip orientation, yet the minor mechanical differences indicated that deformation was chiefly governed by microstructural strengthening rather than texture.

- The higher fraction of the α phase and greater dislocation density in the horizontally built sample, together with the presence of smaller pores and a refined microstructure characterized by a lower Schmid factor, resulted in a partial increase in the surface hardness compared to the vertically built specimen.
- The wear path of the Ti6242 alloy exhibited numerous grooves, indicating that abrasive wear was the primary mechanism. At 450 °C, the COF was lower than at 250 °C and similar to the COF observed at room temperature (~0.5). The improved COF at 450 °C, relative to 250 °C, can be ascribed to the higher oxygen concentration, fostering the formation of more stable titanium oxide with self-lubricating properties. Despite differences in hardness and microstructure, both orientations exhibited comparable wear behaviour under a 5 N load, confirming near isotropic wear resistance. This isotropy resulted from the combined effects of surface finishing and balanced shear response in both directions.

Acknowledgements We express our appreciation to the Integrated Additive Manufacturing Center at Politecnico di Torino, where sample production was conducted. Furthermore, we acknowledge the valuable support received from Politecnico di Bari, where the mechanical and tribological tests were undertaken. We also express our appreciation to the Marine Additive Manufacturing Centre of Excellence (MAMCE) at the University of New Brunswick for their support in conducting the EBSD analysis.

Author contributions Farideh Davoodi: Methodology, Formal analysis, Investigation, Visualization. Writing—Original Draft, Mohammad Taghian: Methodology, Formal analysis, Investigation, Validation, Writing, Parisa Moazzen: Specimen preparation, data acquisition, measurements, Manuela Galati: Investigation, Mohsen Mohammadi: Supervision, Resources, Review & Editing, Abdollah Saboori: Conceptualization, Supervision, Production of all Samples, Validation, Project administration, Resources, Writing—Review & Editing.

Funding Open access funding provided by Politecnico di Torino within the CRUI-CARE Agreement.

Data availability No datasets were generated or analysed during the current study.

Declarations

Conflict of interest The authors declare no financial or commercial conflict of interest.

Open Access This article is licensed under a Creative Commons Attribution 4.0 International License, which permits use, sharing, adaptation, distribution and reproduction in any medium or format, as long as you give appropriate credit to the original author(s) and the source, provide a link to the Creative Commons licence, and indicate if changes were made. The images or other third party material in this article are included in the article's Creative Commons licence, unless indicated otherwise in a credit line to the material. If material is not included in the article's Creative Commons licence and your intended use is not permitted by statutory regulation or exceeds the permitted use, you will need to obtain permission directly from the copyright holder. To view a copy of this licence, visit http://creativecommons.org/licenses/by/4.0/.

References

1. Fan H, Wang C, Tian Y, Zhou K, Yang S (2023) Laser powder bed fusion (L-PBF) of Ti–6Al–4V/Ti–6Al–2Sn–4Zr–2Mo and Ti–6Al–4V/γ-TiAl bimetals: Processability, interface and mechanical properties. Mater Sci Engineering: A 871:144907
2. Chen Y, Clark SJ, Sinclair L, Leung CLA, Marussi S, Connolley T et al (2021) Synchrotron X-ray imaging of directed energy deposition additive manufacturing of titanium alloy Ti-6242. Additive Manuf 41:101969
3. Gogia A (2005) High-temperature titanium alloys. Def Sci J 55:149–173
4. Fan H, Yang S (2020) Effects of direct aging on near-alpha Ti–6Al–2Sn–4Zr–2Mo (Ti-6242) titanium alloy fabricated by selective laser melting (SLM). Mater Sci Engineering: A 788:139533
5. Galati M, Defanti S, Saboori A, Rizza G, Tognoli E, Vincenzi N et al (2022) An investigation on the processing conditions of Ti-6Al-2Sn-4Zr-2Mo by electron beam powder bed fusion: Microstructure, defect distribution, mechanical properties and dimensional accuracy. Additive Manuf 50:102564
6. Du D, Zhang W, An J (2022) Two types of wear mechanisms governing transition between mild and severe wear in Ti-6Al-4V alloy during dry sliding at temperatures of 20–250° C. Materials 15:1416
7. Wang L, Zhang Q, Li X, Cui X, Wang S (2014) Severe-to-mild wear transition of titanium alloys as a function of temperature. Tribol Lett 53:511–520
8. Xu R, Zhu Y, Wu J, Huang P, Wu M, Wang W et al (2025) Hybrid high-temperature wear mechanisms of additive manufactured Ti-6Al-4V alloy. Tribol Int 205:110559
9. Jin J, Zhou S, Zhao Y, Zhang Q, Wang X, Li W et al (2021) Refined microstructure and enhanced wear resistance of titanium matrix composites produced by selective laser melting. Opt Laser Technol 134:106644
10. Briffod F, Bleuset A, Shiraiwa T, Enoki M (2019) Effect of crystallographic orientation and geometrical compatibility on fatigue crack initiation and propagation in rolled Ti-6Al-4V alloy. Acta Mater 177:56–67
11. Roshani M, Abedi HR, Saboori A (2024) Comparing the Cold, Warm, and Hot Deformation Flow Behavior of Selective Laser-Melted and Electron-Beam-Melted Ti–6Al–2Sn–4Zr–2Mo Alloy. Adv Eng Mater 26:2301046
12. Taghian M, Mani H, Mosallanejad M, Abdi A, Saboori A, Iuliano L (2024) Critical condition for initiation of dynamic recrystallisation in electron beam powder bed fused Ti-6Al-4V alloy. J Alloys Compd 1005:176165
13. Landau E, Tiferet E, Ganor Y, Ganeriwala R, Matthews M, Braun D et al (2020) Thermal characterization of the build chamber in electron beam melting. Additive Manuf 36:101535
14. Aiza I, Baldi C, de la Vega FM, Sebastiani S, Veronese NE, Yousefi M et al (2024) Effects of build orientation and inclined

features on physical, microstructural and mechanical properties of powder bed fusion additively manufactured metallic parts. Prog Mater Sci 147:101357
15. Kok Y, Tan XP, Wang P, Nai M, Loh NH, Liu E, Tor SB (2018) Anisotropy and heterogeneity of microstructure and mechanical properties in metal additive manufacturing: A critical review. Mater Design 139:565–586
16. Davoodi F, Taghian M, Carbone G, Saboori A, Iuliano L (2023) An Overview of the Latest Progress in Internal Surface Finishing of the Additively Manufactured Metallic Components. Materials 16:3867
17. Riaz MQ, Caputo M, Ferraro MM, Ryu JJ (2018) Influence of process-induced anisotropy and synovial environment on wear of EBM built Ti6Al4V joint implants. J Mater Eng Perform 27:3460–3471
18. Yang Y, Zhu Y, Khonsari M, Yang H (2019) Wear anisotropy of selective laser melted 316L stainless steel. Wear 428:376–386
19. Chen Y, Zhao X, Liu P, Pan R, Ren R (2018) Influences of local laser quenching on wear performance of D1 wheel steel. Wear 414:243–250
20. Moazzen P, Toroghinejad M, Aghayar Y, Zargar T, Davoodi F, Mohammadi M (2024) Exploring Nanocrystalline High Entropy Alloys Fabricated via Mechanical Alloying (MA) and Spark Plasma Sintering (SPS): A Review. High Entropy Alloys Mater 2:175–218
21. Lizzul L, Sorgato M, Bertolini R, Ghiotti A, Bruschi S (2020) Influence of additive manufacturing-induced anisotropy on tool wear in end milling of Ti6Al4V. Tribol Int 146:106200
22. Podgornik B, Šinko M, Godec M (2021) Dependence of the wear resistance of additive-manufactured maraging steel on the build direction and heat treatment. Additive Manuf 46:102123
23. Walker K, Liu Q, Brandt M (2017) Evaluation of fatigue crack propagation behaviour in Ti-6Al-4V manufactured by selective laser melting. Int J Fatigue 104:302–308
24. Hadadzadeh A, Amirkhiz BS, Li J, Mohammadi M (2018) Columnar to equiaxed transition during direct metal laser sintering of AlSi10Mg alloy: effect of building direction. Additive Manuf 23:121–131
25. Fan H, Witvrouw A, Wolf-Monheim F, Souschek R, Yang S (2023) Effects of substrate surface treatments on hybrid manufacturing of AlSi7Mg using die casting and selective laser melting. J Mater Sci Technol 156:142–156
26. Krasnova E, Morgunov YA, Saushkin B, Khomyakova N (2023) Properties of Ti–6Al–4V alloy powders for selective electron-beam additive manufacturing of products. Russ Metall 2023:1952–1959
27. Sola A, Nouri A (2019) Microstructural porosity in additive manufacturing: The formation and detection of pores in metal parts fabricated by powder bed fusion. J Adv Manuf Process 1:e10021
28. Nezhadfar P, Thompson S, Saharan A, Phan N, Shamsaei N (2021) Structural integrity of additively manufactured aluminum alloys: Effects of build orientation on microstructure, porosity, and fatigue behavior. Additive Manuf 47:102292
29. Al-Maharma AY, Patil SP, Markert B (2020) Effects of porosity on the mechanical properties of additively manufactured components: a critical review. Mater Res Express 7:122001
30. Ghods S, Schur R, Schultz E, Pahuja R, Montelione A, Wisdom C et al (2021) Powder reuse and its contribution to porosity in additive manufacturing of Ti6Al4V. Materialia 15:100992
31. Mindt H-W, Desmaison O, Megahed M, Peralta A, Neumann J (2018) Modeling of powder bed manufacturing defects. J Mater Eng Perform 27:32–43
32. Luo Q, Yin L, Simpson TW, Beese AM (2022) Effect of processing parameters on pore structures, grain features, and mechanical properties in Ti-6Al-4V by laser powder bed fusion. Additive Manuf 56:102915
33. Yuan T, Ren X, Chen S, Jiang X (2022) Grain refinement and property improvements of Al–Zn–Mg–Cu alloy by heterogeneous particle addition during wire and arc additive manufacturing. J Mater Res Technol 16:824–839
34. Islam MA, Farhat ZN (2011) Effect of porosity on dry sliding wear of Al–Si alloys. Tribol Int 44:498–504
35. Delfs P, Tows M, Schmid H-J (2016) Optimized build orientation of additive manufactured parts for improved surface quality and build time. Additive Manuf 12:314–320
36. Yan X, Gao S, Chang C, Huang J, Khanlari K, Dong D et al (2021) Effect of building directions on the surface roughness, microstructure, and tribological properties of selective laser melted Inconel 625. J Mater Process Technol 288:116878
37. Steen WM, Mazumder J (2010) Laser material processing. Springer science & business media
38. Xie Z, Dai Y, Ou X, Ni S, Song M (2020) Effects of selective laser melting build orientations on the microstructure and tensile performance of Ti–6Al–4V alloy. Mater Sci Engineering: A 776:139001
39. Chen W-Y, Liu X, Chen Y, Yeh J-W, Tseng K-K, Natesan K (2018) Irradiation effects in high entropy alloys and 316H stainless steel at 300 C. J Nucl Mater 510:421–430
40. Sidor JJ, Chakravarty P, Bátorfi JG, Nagy P, Xie Q, Gubicza J (2021) Assessment of dislocation density by various techniques in cold rolled 1050 aluminum alloy. Metals 11:1571
41. Ahmed MT, Islam S, Bashar MS, Hossain MA, Ahmed F (2022) Synthesis and characterizations of CH3NH3PbI3: ZnS microrods for optoelectronic applications. Adv Mater Sci Eng 2022:7606339
42. Kumar D, Shankar G, Prashanth K, Suwas S (2021) Texture dependent strain hardening in additively manufactured stainless steel 316L. Mater Sci Engineering: A 820:141483
43. Aly KA, Khalil N, Algamal Y, Saleem QM (2017) Estimation of lattice strain for zirconia nano-particles based on Williamson-Hall analysis. Mater Chem Phys 193:182–188
44. Bertsch K, De Bellefon GM, Kuehl B, Thoma D (2020) Origin of dislocation structures in an additively manufactured austenitic stainless steel 316L. Acta Mater 199:19–33
45. Prashanth K, Eckert J (2017) Formation of metastable cellular microstructures in selective laser melted alloys. J Alloys Compd 707:27–34
46. Dixit S, Liu S, Murdoch HA, Smith PM (2023) Investigating build orientation-induced mechanical anisotropy in additive manufacturing 316L stainless steel. Mater Sci Engineering: A 880:145308
47. Razavi SMJ, Van Hooreweder B, Berto F (2020) Effect of build thickness and geometry on quasi-static and fatigue behavior of Ti-6Al-4V produced by Electron Beam Melting. Additive Manuf 36:101426
48. Mosallanejad MH, Niroumand B, Ghibaudo C, Biamino S, Salmi A, Fino P, Saboori A (2022) In-situ alloying of a fine grained fully equiaxed Ti-based alloy via electron beam powder bed fusion additive manufacturing process. Additive Manuf 56:102878
49. Al-Bermani S, Blackmore M, Zhang W, Todd I (2010) The origin of microstructural diversity, texture, and mechanical properties in electron beam melted Ti-6Al-4V. Metall Mater Trans A 41:3422–3434
50. Wang M, Li H, Lou D, Qin C, Jiang J, Fang X, Guo Y (2019) Microstructure anisotropy and its implication in mechanical properties of biomedical titanium alloy processed by electron beam melting. Mater Sci Engineering: A 743:123–137
51. Yang KV, Shi Y, Palm F, Wu X, Rometsch P (2018) Columnar to equiaxed transition in Al-Mg (-Sc)-Zr alloys produced by selective laser melting. Scripta Mater 145:113–117
52. Yang J, Yu H, Wang Z, Zeng X (2017) Effect of crystallographic orientation on mechanical anisotropy of selective laser melted Ti-6Al-4V alloy. Mater Charact 127:137–145

53. Dharmendra C, Hadadzadeh A, Amirkhiz B, Lloyd A, Mohammadi M (2020) Deformation mechanisms and fracture of electron beam melted Ti–6Al–4V. Mater Sci Engineering: A 771:138652
54. Kaushik HC, Shakerin S, Korayem MH, Mohammadi M, Hadadzadeh A (2025) Competing roles of microstructure and defects on the mechanical properties of laser-powder bed fused Ti-6Al-2Sn-4Zr-2Mo alloy. Progress Additive Manuf 10:1605–1627
55. Hassan N, Lee J, Kim M, Kim U, Kim M, Moon S et al (2024) Enhanced mechanical properties of aluminum nitride-yttria ceramics through grain refinement by pressure assisted two-step sintering. J Eur Ceram Soc 44:831–840
56. Ju J, Zhou Y, Wang K, Liu Y, Li J, Kang M, Wang J (2020) Tribological investigation of additive manufacturing medical Ti6Al4V alloys against Al2O3 ceramic balls in artificial saliva. J Mech Behav Biomed Mater 104:103602
57. Khorasani A, Gibson I, Awan US, Ghaderi A (2019) The effect of SLM process parameters on density, hardness, tensile strength and surface quality of Ti-6Al-4V. Additive Manuf 25:176–186
58. Ge J, Ma T, Chen Y, Jin T, Fu H, Xiao R et al (2019) Wire-arc additive manufacturing H13 part: 3D pore distribution, microstructural evolution, and mechanical performances. J Alloys Compd 783:145–155
59. Fantetti A, Tamatam LR, Volvert M, Lawal I, Liu L, Salles L et al (2019) The impact of fretting wear on structural dynamics: Experiment and Simulation. Tribol Int 138:111–124
60. Li H, Chen ZW, Ramezani M (2022) Effect of temperature on sliding wear behavior of Ti-6Al-4V alloy processed by powder bed fusion additive manufacturing techniques. J Mater Eng Perform 31:8940–8954
61. Jeffs S, Lancaster R, Davies G, Hole W, Roberts B, Stapleton D et al (2021) Effect of process parameters and build orientation on microstructure and impact energy of electron beam powder bed fused ti-6al-4v. Materials 14:5376
62. Wood P, Libura T, Kowalewski ZL, Williams G, Serjouei A (2019) Influences of horizontal and vertical build orientations and post-fabrication processes on the fatigue behavior of stainless steel 316l produced by selective laser melting. Materials 12:4203
63. Davoodi F, Atapour M, Ashrafizadeh F, Rikhtehgaran R (2022) Dry Sliding Wear Characteristics of NiP/TiN Duplex Coated Aluminum Alloy and Wear Analysis Using Response Surface Method. J Mater Eng Perform 31:6360–6372
64. Ren Y, Liu X, Wang H, Yang Y, Baker I, Wang P, Wu H (2023) Unraveling the inherent anisotropic properties of in situ alloyed copper-modified titanium alloys produced by laser powder bed fusion. J Alloys Compd 966:171323
65. Davoodi F, Ashrafizadeh F, Atapour M, Rikhtehgaran R (2022) A novel approach for evaluation of load bearing capacity of duplex coatings on aluminum alloy using PLS and SVR models. Trans Nonferrous Met Soc China 32:1834–1851
66. Guglielmi P, Davoodi F, Palumbo G, Carbone G (2024) Tribological behaviour of microindented 100Cr6 steel surfaces in dry contact conditions. Int J Adv Manuf Technol 133(5):2381–2400
67. Yetim A (2010) Investigation of wear behavior of titanium oxide films, produced by anodic oxidation, on commercially pure titanium in vacuum conditions. Surf Coat Technol 205:1757–1763
68. Wu L, Luo K, Liu Y, Cui C, Xue W, Lu J (2018) Effects of laser shock peening on the micro-hardness, tensile properties, and fracture morphologies of CP-Ti alloy at different temperatures. Appl Surf Sci 431:122–134
69. Davoodi F, Varmaziar S, Atapour M, Iuliano L, Saboori A (2025) In vitro corrosion and bio-tribocorrosion performance of electron beam powder bed fusion Ti6Al4V specimens with lapping and superfinishing treatments. Progress Additive Manuf 10(11):9117–9132
70. Kubiak K, Liskiewicz T, Mathia T (2011) Surface morphology in engineering applications: Influence of roughness on sliding and wear in dry fretting. Tribol Int 44:1427–1432
71. List G, Sutter G, Arnoux J, Molinari A (2015) Study of friction and wear mechanisms at high sliding speed. Mech Mater 80:246–254
72. Cai Y, Wu H, Luo S (2018) A loading-dependent model of critical resolved shear stress. Int J Plast 109:1–17
73. Rigney D (1997) Comments on the sliding wear of metals. Tribol Int 30:361–367
74. Aghababaei R, Warner DH, Molinari J-F (2016) Critical length scale controls adhesive wear mechanisms. Nat Commun 7:11816
75. Brink T, Molinari J-F (2019) Adhesive wear mechanisms in the presence of weak interfaces: Insights from an amorphous model system. Phys Rev Mater 3:053604

Publisher's note Springer Nature remains neutral with regard to jurisdictional claims in published maps and institutional affiliations.